Time-periodic forcing in a Cahn-Hilliard model for Langmuir-Blodgett transfer

Master's Thesis submitted

to

Prof. Dr. Svetlana V. Gurevich
Prof. Dr. Uwe Thiele

Westfälische-Wilhelms-Universität Münster
Institut für Theoretische Physik

by

Phong-Minh Timmy Ly

Münster, September 2017

Contents

1 Introduction

Surface patterning is done in many fields of science and industry. The majority of these patterning techniques can be classified as either *top-down* or *bottom-up* methods. In the narrower sense photolithographic methods belong to *top-down* methods where essentially a light-sensitive polymer (photo-resist) is exposed to UV light following a pattern. The photo-resist becomes easier to remove on the exposed parts, thus forming the basis for subsequent patterning processes like engraving [PS12]. Micro- and nanolithography have uses in various fields, e.g. plasmonics [Ozb06, HLL$^+$09], biology [YRP$^+$05] and electronics [IO00]. On the other hand, a widely used bottom-up patterning technique is *dip-coating* [Wil82, WJ04, SADF07, DFSA08]. A substrate is dipped into a liquid bath and then pulled out with the intention of coating the substrate with the liquid. The latter can also be a solution or covered with *surfactants*. Surfactants are surface active agents and they usually are organic molecules with a hydrophilic head and hydrophobic tail (amphiphilic).
A subcategory of dip-coating techniques is the *Langmuir-Blodgett transfer* (shortened: LB-transfer) [Lan34, Blo34, Blo35]. Here it is not necessarily a homogeneous film that is transferred onto the substrate. The experimental setup can be seen in Fig. 1 and is described in the following.

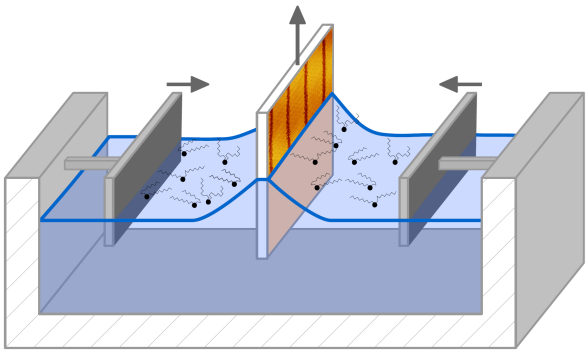

Figure 1: Sketch of a Langmuir-Blodgett trough covered by a monolayer of spread out surfactants. A substrate is pulled out of the trough and the molecules are deposited onto the substrate forming different kinds of patterns depending on whether a phase transition occurs. Barriers on the sides are pushed towards the substrate during the process in order to keep the molecular surface density constant. ([Wil16])

The liquid bath specifically is covered by a monolayer of surfactants which are spread out on the surface. This is called the *liquid-expanded* phase. If they arrange themselves closely in an organized manner with their hydrophilic heads pointing perpendicular to the surface, they are in the *liquid-condensed* phase (see Fig: 2). Upon pulling out the substrate, the molecules do not necessarily transfer as a homogeneous LE phase. Close to the three-phase contact line so-called substrate-mediated condensation sets in ([KGFC10, SCR93, GR96, LBM00]).

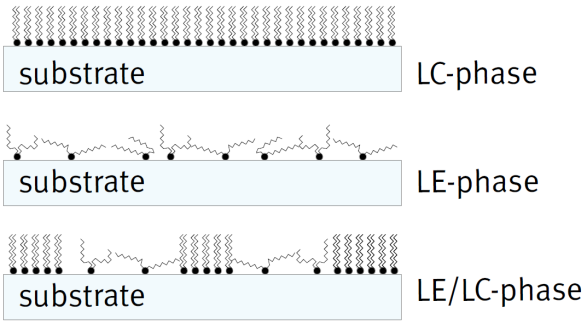

Figure 2: Sketches of surfactant phases in LB-transfer. Top: Surfactants are ordered perpendicular to the substrate with the hydrophilic head facing downwards (LC phase). Middle: Surfactants are spread across the substrate (LE phase). Bottom: Alternating LE/LC phase [Wil12]

.

This is an effect caused by the interaction between surfactants and substrate which favors a phase transition from LE to LC phase upon deposition of the molecules and can result in different kinds of patterns on the substrate. Which kind of pattern is transferred depends on control parameters, e.g. the velocity with which the substrate is withdrawn (*transfer velocity*). For a certain range of velocities patterns of alternating LE and LC phase are transferred. AFM images of such patterns are depicted in Fig. 3 where L-α-dipalmitoylphosphatidylcholine molecules (DPPC) are transferred onto mica substrates. From left to right the transfer velocity is increased and the transfer direction goes from bottom to top. Stripes which are aligned parallel to the transfer direction will be called *vertical stripes* from now on and those which are aligned perpendicularly will be called *horizontal stripes*. Rectangular patterns can be observed as well. For sufficiently high (or low) velocities purely LE phase (or purely LC phase) layers are transferred.

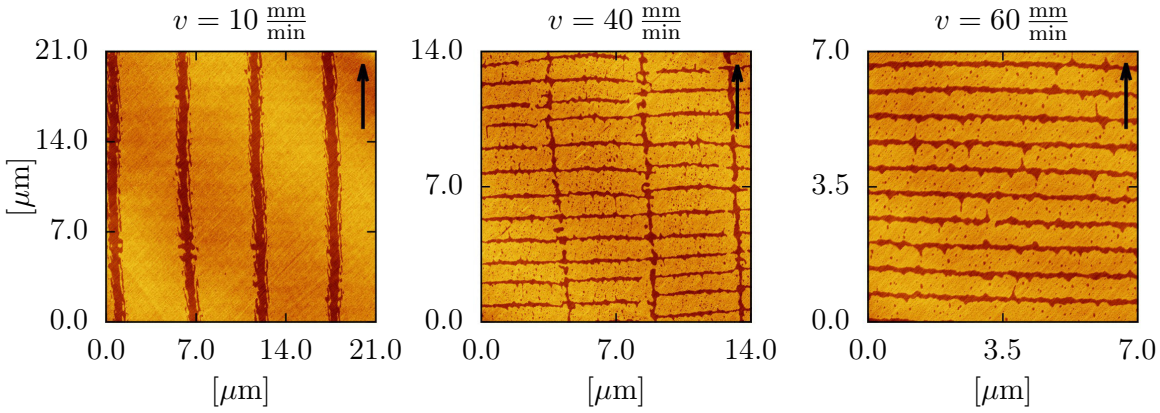

Figure 3: AFM images of various pure DPPC patterns on mica surfaces for increasing transfer velocities v ([CLH$^+$]).

What is remarkable is that the patterns can exhibit high regularity over several cm^2 with the stripe widths being around the orders of several hundred nm [CLH$^+$]. This underlines the cost efficiency aspect of LB-transfer regarding deposition of μm sized patterns on larger scales. Unfortunately, this regularity cannot be always achieved. "Rayleigh instability, structural defects on the substrate or impurities on the water surface" [ZWH$^+$16] can especially cause vertical stripes to form branched structures as can be seen in Fig. 4 (a).

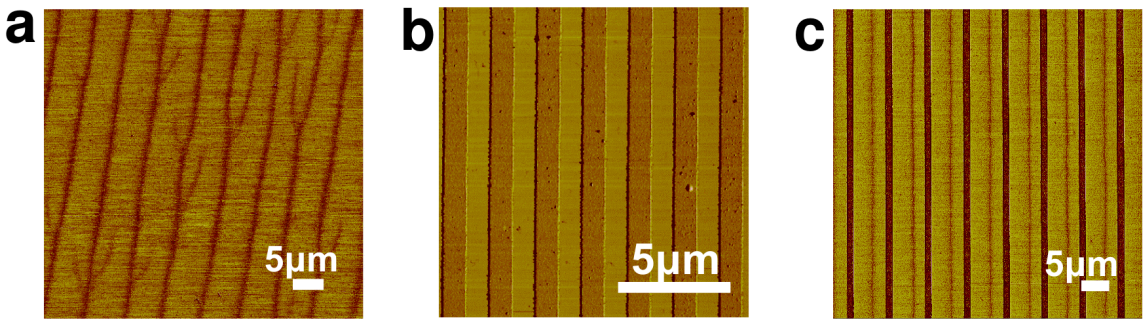

Figure 4: AFM images obtained from LB-transfer with the same transfer velocities. Dark brown represents LE and light brown LC phase. (a) Vertical stripes with branches in the case of no prestructures. (b,c): Well-defined vertical stripes in the case of vertically striped prestructured surface and line spacing of (b) $1\mu m$ and (c) $6\mu m$ ([ZWH$^+$16]).

An effective way of stabilizing regular patterns and suppressing branched structures is the introduction of spatial forcing via prestructured substrates. This means that a property of the substrate, e.g. the wettability, is periodically modulated in space by modifying the substrate. Two exemplary stripe patterns are shown in Fig. 4 (b) and (c) for vertically striped prestructures with two different line spacings. One can see that the branched structures are effectively suppressed and well-defined vertical stripes are formed. In addition, synchronization effects can occur, meaning that the stripe width locks onto the width of the prestructures in a rational manner. Therefore, it is also possible to induce patterns that are finer than the prestructure is. So prestructures can not only stabilize regular patterns but also be a means to actually control the stripe width. Further details on synchronization effects will be discussed in Sec. 2.2.

One disadvantage of using prestructures as external forcing of the system is the cost that is involved in creating them. If they are created by depositing material onto the substrate, then the costs will only increase with the desired amount of patterned structures. The natural analogue to spatial forcing is temporal forcing which does not necessitate modifications of the substrate. Thus, since spatial forcing is proven to be effective, temporal forcing might work as well. This thesis investigates the behavior of a Cahn-Hilliard model for the LB-transfer which has been established in previous works [KGFC10, KGFT12, KT14]. Here, in contrast, the transfer velocity will be subject to a time-periodic forcing term. Another modification of the model with a prestructure description has been investigated in [Wil12, WG14, Wil16]. The pattern formation in LB-transfer was first modelled via a hydrodynamic approach [KGFC10] and later reduced to a Cahn-Hilliard model. In the original approach the local film height $H(x,y,t)$ and the surfactant density $\Gamma(x,y,t)$ are modelled by the following set of two partial differential equations:

$$\begin{aligned}\partial_t H(x,y,t) = -\nabla\cdot\Bigg[&\frac{H^3}{3}\nabla\left((1-\epsilon^2 P_{\text{hom}})\Delta H - \Pi\right)\\ &+\frac{H^2}{2}(\epsilon^{-2}\Gamma\nabla\Delta\Gamma - \nabla P_{\text{hom}}) - H\mathbf{v}\Bigg] + Q\end{aligned} \tag{1}$$

$$\begin{aligned}\partial_t \Gamma(x,y,t) = -\nabla\cdot\Bigg[&\frac{\Gamma H^2}{2}\nabla\left((1-\epsilon^2 P_{\text{hom}})\Delta H - \Pi\right)\\ &+\Gamma H\left(\epsilon^{-2}\Gamma\nabla\Delta\Gamma - \nabla P_{\text{hom}}\right) - \Gamma\mathbf{v}\Bigg]\end{aligned} \tag{2}$$

Each first term on the right hand side of Eq. (1) and (2) is a *generalized pressure gradient* composed of *laplace pressure* proportional to *surface curvature* ΔH and *disjoining pressure*

$\Pi(H)$. The latter describes the wetting properties of the substrate. $P_{\mathrm{Hom}}(\Gamma)$ is the surface pressure for a homogeneous surfactant layer with density Γ. Q breaks mass-conservation and represents evaporation of the liquid. $\nabla \cdot H\mathbf{v}$ and $\nabla \cdot \gamma\mathbf{v}$ are advection terms. The rest of the terms in the respective second lines of Eq. (1) and (2) are Marangoni forces caused by surface tension gradients that appear from the spatial inhomogeneity of Γ. Note, that (2) is a conserved equation and thus a free energy functional can be derived which is of the Cahn-Hilliard-type.

It turns out that the meniscus dynamics do not play a significant role regarding the behavior of pattern formation in this model. Even with an artificially frozen contact line the phase transition from LE to LC phase or its decomposition still occurs [KGFT12]. Therefore it is possible to reduce the model to a Cahn-Hilliard equation solely describing the phase decomposition.

This thesis is structured into six parts. Following this introductory section, the Cahn-Hilliard equation and its modifications will be derived. Furthermore, relevant synchronization phenomena will be discussed. In Sec. 3 the numerical implementation is outlined before presenting the results and findings from numerical simulations of the model (9) with time-periodic forcing in Sec. 4 and 5. In the end a summary is given together with an outlook on aspects that need more investigation.

2 Theoretical background

2.1 Mathematical model

Let $c(\mathbf{x}, t)$ be a molecular concentration field. The generalized Cahn-Hilliard equation is a continuity equation with flow $\mathbf{J}$ which is mainly determined by the gradient of the functional derivative of a free energy $\mathcal{F}$. Thus, c is conserved. $M(c)$ is the mobility.

$$\partial_t\, c(\mathbf{x}, t) = -\nabla \cdot \mathbf{J} = -\nabla \cdot \left(M(c) \nabla \frac{\delta \mathcal{F}[c]}{\delta c} \right). \tag{3}$$

The CH-equation describes phase separation where the dynamics are largely determined by the free energy functional which has the following form [NCS84]:

$$\mathcal{F}[c] = \int_\Omega \frac{\kappa}{2} |\nabla c|^2 + f(c) d\mathbf{x} \tag{4}$$

The domain Ω is at most two-dimensional for our system. In LB-transfer patterns form when the LE phase undergoes a phase transition upon entraining on the substrate. Especially the patterns of alternating LC/LE phase remind of spinodal decomposition of a binary mixture. This can be described with a Cahn-Hilliard equation. Specifically by choosing the free local energy as a double-well potential.

$$f(c) = a_1 c^2 + a_2 c^4 \tag{5}$$

Setting $a_1 = \frac{1}{4}$ and $a_2 = -\frac{1}{2}$ shifts the minima of $f(c)$ to $c = \pm 1$ which represent coexistent states during phase separation in Eq. (3) respectively. Next, the substrate-mediated condensation (SMC), which favors the phase transition from LE to LC, needs to be incorporated. This is done by introducing the SMC-term

$$\zeta(x) = -\frac{1}{2} \left(1 + \tanh \left(\frac{x - x_s}{l_s} \right) \right) \tag{6}$$

to the free local energy

$$f(c, x) = \frac{c^2}{4} - \frac{c^4}{2} + \mu \zeta(x) c. \tag{7}$$

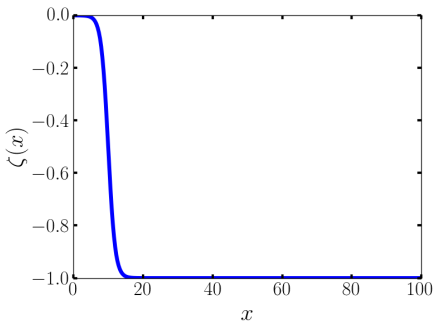

Figure 5: Plot of SMC-term according to Eq. (6).

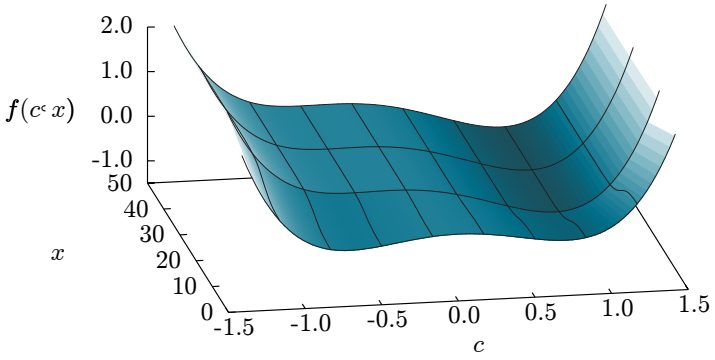

Figure 6: 3D plot of the free local energy $f(c)$ with SMC-term (7) [[Wil12]].

x_s is the meniscus position and μ regulates the strength of ζ. The tanh-term is used in order to smoothly transition the system from vanishing to existing interaction. l_s is the width of the transition. ζ effectively shifts the $c = 1$ minimum in $f(c, x)$ to lower values and the one

at $c = -1$ to higher ones the further away one moves from the contact line (see Fig. 6). Inserting Eq. (7), (4) into (3) results in

$$\partial_t\, c(\mathbf{x},t) = -\nabla \cdot \left[-\nabla\left(-\Delta c - c + c^3 + \mu\zeta(x)\right)\right] \tag{8}$$

On the last step we introduce an advection term $\mathbf{v}\cdot\nabla c$ in order to model the withdrawal of the substrate while focusing the frame of reference around the contact line where the patterns form

$$\partial_t\, c(\mathbf{x},t) = -\nabla \cdot \left[-\nabla\left(-\Delta c - c + c^3 + \mu\zeta(x)\right) - \mathbf{v}c\right]. \tag{9}$$

$$\zeta(x) = -\frac{1}{2}\left(1 + \tanh\left(\frac{x - x_s}{l_s}\right)\right) \tag{10}$$

Equation (9) is the model which is being investigated in this thesis with the following boundary conditions:

$$c(0,y) = c_0, \qquad \partial_{xx}c(0,y) = \partial_x c(L,y) = \partial_{xx}c(L,y) = 0 \tag{11}$$

$c(0) = c_0 = -0.9$ represents the continuous influx of LE phase from the left boundary of the domain. In the 2D case periodic boundary conditions are chosen in the y-direction.
In this thesis, if not said otherwise, the following initial condition, representing a simple frozen meniscus, will always be used:

$$c(x,y,0) = c_0 + \frac{1}{2}(1 + \tanh(x - x_s))(1 - c_0). \tag{12}$$

In addition, the following L^2-norm is used:

$$||c(x,y)||^2 = \frac{1}{L_x L_y}\int_0^{L_x}\int_0^{L_y} c(x,y)^2 dxdy. \tag{13}$$

2.2 Synchronization

The following derivations closely follow [RP03] We consider a system with a stable limit cycle solution. It is possible to define a *phase* variable $\varphi(t)$, which increases in time with constant frequency Ω_{nat}, such that the solution has traversed the whole limit cycle after one period of $\varphi(t)$. So the phase follows

$$\frac{d\varphi}{dt} = \Omega_{\text{nat}}. \tag{14}$$

and

$$\varphi(t) = \varphi(t + nT) + 2n\pi. \tag{15}$$

Ω is the *natural frequency* of the system. Since it is constant in time, changes in φ, for example by perturbations, remain. This means that the phase is *neutrally stable*.
Next, a periodic, external force Q with *amplitude* A and *frequency* ω is introduced to the system. It affects the phase dynamics in particular

$$\frac{d\varphi}{dt} = \Omega_{\text{nat}} + A \cdot Q(\varphi, \omega t). \tag{16}$$

If Ω is close to the forcing frequency ω, meaning $\Omega \approx \omega$, then the external force is mainly governed by the *phase difference* $\psi = \varphi - \omega t$ and we can rewrite Eq. (16) into

$$\frac{d\psi}{dt} = -(\omega - \Omega_{\text{nat}}) + Aq(\psi), \tag{17}$$

with the redefined forcing $q(\psi)$. In the simplest case q is a sine function, turning Eq. (17) into the *Adler* equation. Setting $\frac{d\psi}{dt} = 0$ so that

$$\omega - \Omega_{\text{nat}} = Aq(\psi), \tag{18}$$

the phase difference ψ becomes stationary for certain pairs of (ω, A) because $q(\psi) = \text{const}$. This also means that φ exactly follows ωt with fixed offset. This is called *phase locking*. The mean frequency $\Omega_0 = < \frac{d\varphi}{dt} >$ of the system is exactly the same as ω so the system is synchronized 1:1 with the forcing. Note that in this case calculating the mean is obsolete because the phases are already locked and ω is constant. The ratio of mean frequency Ω_0 and forcing frequency is also called rotation number, winding number or *synchronization order*

$$W = \frac{\Omega_0}{\omega} = \frac{n}{m} \qquad n, m \,\epsilon\, \mathbb{N}. \tag{19}$$

Generally, externally forced systems with intrinsic natural frequencies can synchronize to many different synchronization orders. In order to include these, Eq. (17) is modified along with a slight redefinition of the phase difference ψ

$$\frac{d\psi}{dt} = -(n\omega - m\Omega) + A\tilde{q}(\psi). \tag{20}$$

This equation has multiple regions in (ω, A)-space where stationary solutions occur. Each region can be classified by a synchronization order $W = \frac{n}{m}$. An example of their appearance is shown in Fig. 7. Starting from small forcing amplitudes A, the regions of synchronization expand with increasing amplitude. For fixed amplitude and varying ω the synchronization order decreases monotonically as can be seen in 8. This is called a *devil's staircase*. It shows that in-between the tongues in Fig. 7 synchronization still occurs, though, higher integer values are involved.

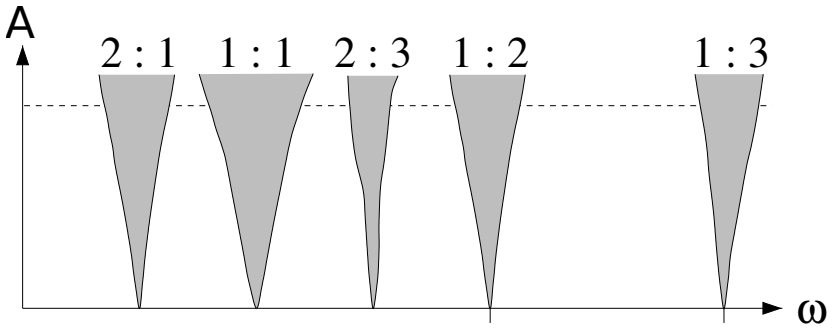

Figure 7: Sketch of Arnold tongues. Largest regions of synchronization are depicted in gray with the corresponding synchronization orders W above. The regions expand with increasing forcing amplitude A. Changing ω for fixed A leads to different synchronization orders ([PRK01]).

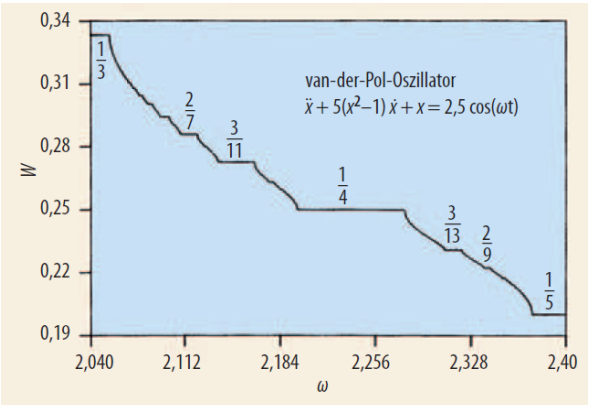

Figure 8: Dependence of synchronization order W on forcing frequency ω for the externally forced van-der-Pol-oscillator. This is called a devil's staircase ([PRK01]).

Two more important aspects about synchronization need to be emphasized here: Synchronization orders comprised of low value integers are favored over high valued ones. Furthermore, the smaller $n\omega - m\Omega$ is, the smaller the amplitude requirement for synchronization becomes (cf. Eq. (20)).

3 Numerical methods

The Cahn-Hilliard equation is a partial differential equation. In order to calculate its solutions different kinds of numerical schemes are necessary.

3.1 Finite difference methods

Let $c(\mathbf{x}, t)$ be the solution of the PDE

$$\frac{\partial c}{\partial t}(\mathbf{x}, t) = f(c(\mathbf{x}, t), t) \ . \tag{21}$$

The right hand side f typically contains spatial derivatives. One way of dealing with PDEs is to discretize the spatial domain on which the solution is evaluated in order to transform the PDE into a system of ordinary differential equations. After that, the system of ODEs is solved via time-integration methods.
First, the domain of dimension L^d needs to be divided into a grid where d is the spatial dimension of the system. If we choose a uniform grid with discretization Δx, then for $d = 1$ each point x_i can be identified by

$$x_i = i\Delta x \qquad i = 1, ..., N_x \ . \tag{22}$$

In this case we choose a domain extending along the positive x-axis and N is the number of grid points. When calculating the solution $c(x, t)$ or its derivatives at one point in time, they are only evaluated on these grid points.

$$c_i := c(x_i) \ . \tag{23}$$

So $c(x_i+\Delta x) = c_{i+1}$. The approximation of the derivatives are derived from Taylor expanding $c(x + \Delta x)$

$$c(x + \Delta x) = c(x) + \frac{\partial c}{\partial x}\Delta x + \frac{1}{2}\frac{\partial^2 c}{\partial x^2}\Delta x^2 + \mathcal{O}(\Delta x^3). \tag{24}$$

Neglecting second order and higher terms, then solving for $\frac{\partial c}{\partial x}$ results in the so called *forward differences* scheme

$$\frac{\partial c}{\partial x} = \frac{c(x + \Delta x) - c(x)}{\Delta x} + \mathcal{O}(\Delta x). \tag{25}$$

The *backward differences* scheme can be derived analogously by replacing Δx with $-\Delta x$

$$\frac{\partial c}{\partial x} = \frac{c(x) - c(x - \Delta x)}{\Delta x} + \mathcal{O}(\Delta x). \tag{26}$$

Adding these equations together and dividing by 2 results in the *central differences* scheme

$$\frac{\partial c}{\partial x} = \frac{c(x + \Delta x) - c(x - \Delta x)}{2\Delta x} + \mathcal{O}(\Delta x^2) \tag{27}$$

which actually has higher accuracy than the other two schemes since the second order terms of the Taylor expansion cancel each other out. If one includes higher order terms in the Taylor expansion it is possible to approximate higher order derivatives and also to achieve higher order accuracy. Going back to the notation with discretized field c_i the central differences scheme for first order derivative with second order accuracy takes the following form:

$$\frac{\partial c}{\partial x}\Big|_{x_i} = \frac{c_{i+1} - c_{i-1}}{2\Delta x} \ . \tag{28}$$

Typically, only the coefficients that are in front of the c_i, including prefactors in the denominator, are listed when discussing finite differences *stencils*. The central finite differences stencils for first, second and fourth order derivatives in one dimension are listed in Tab. 1 with second order accuracy.

		Grid point index				
Derivative	Accuracy	2	1	0	−1	−2
1	2	0	$\frac{1}{2}$	0	$-\frac{1}{2}$	0
2	2	0	1	−2	1	0
4	2	1	−4	6	−4	1

Table 1: Coefficients for central finite differences of second order accuracy and first, second, fourth derivative in one dimension.

Finite differences approximations can be done for higher dimensional fields like $c(x_i, y_j) := c_i^j$ as well. The corresponding Laplacian and biharmonic operator in second order accuracy are mentioned here without derivation:

$$\Delta c(x,y)\,|_{x_i,y_j} = \frac{c_{i+1}^{j+1} + c_{i+1}^{j} + c_{i+1}^{j-1} + c_{i}^{j+1} - 8c_i^j + c_i^{j-1} + c_{i-1}^{j+1} + c_{i-1}^{j} + c_{i-1}^{j-1}}{3\Delta x} + \mathcal{O}(\Delta x^2) \tag{29}$$

$$\begin{aligned}\Delta^2 c(x,y)\,|_{x_i,y_j} = \frac{1}{\Delta x^4}\Big(& c_{i+2}^{j} + 2c_{i+1}^{j+1} - 8c_{i+1}^{j} + 2c_{i+1}^{j-1} + c_i^{j+2} - 8c_i^{j+1} + 20c_i^j - 8c_i^{j-1} \\ & + c_i^{j-2} + 2c_{i-1}^{j+1} - 8c_{i-1}^{j} + 2c_{i-1}^{j-1} + 2c_{i-2}^{j}\Big) + \mathcal{O}(\Delta x^2).\end{aligned} \tag{30}$$

3.1.1 Boundary conditions and virtual grid points

When straightforwardly using central finite differences the question of how to deal with derivatives on the outer most points will arise since for example c_{N+1} is not defined. One could directly implement forward and backward finite differences to circumvent that, however, there is another method which conveniently implements boundary conditions as well. In particular it is by extending the grid to *virtual grid points* that are not subject to the time integration.
We recall the boundary conditions for the specific Cahn-Hilliard model in Eq. (11):

$$c(0,y) = c_0, \qquad \partial_{xx} c(0,y) = \partial_x c(L,y) = \partial_{xx} c(L,y) = 0 \tag{31}$$

and first consider the lower boundary at $x = 0$. $c(0) = c_0$ is easily implemented by directly setting $c_0^j = c_0$. For $\partial_{xx} c(0,y) = 0$ we recall the central finite differences coefficients from Tab. 1

$$\frac{\partial^2 c}{\partial x^2}\,|_{x_0,y_j} = \frac{c_1^j - 2c_0^j + c_{-1}^j}{\Delta x} \tag{32}$$

Applying $\frac{\partial^2 c}{\partial x^2} = 0$ and solving for c_{-1}^j results in the condition

$$c_{-1}^j = 2c_0^j - c_1^j. \tag{33}$$

The upper boundaries

$$\partial_x c(L,y) = \partial_{xx} c(L,y) = 0 \tag{34}$$

can be implemented by indirectly using forward differences as follows:

$$\frac{\partial c}{\partial x}\Big|_{x_N,y} = \frac{c_{N+2}^j - c_N^j}{2\Delta x} + \mathcal{O}(\Delta x^2) \tag{35}$$

$$\frac{\partial^2 c}{\partial x^2}\Big|_{x_N,y} = \frac{c^j_{N+2} - 2c^j_{N+1} + c^j_N}{2\Delta x} + \mathcal{O}(\Delta x^2). \tag{36}$$

Applying Eq. 34 results in

$$c^j_{N+2} = c^j_{N+1} = c_N. \tag{37}$$

Periodic boundary conditions are implemented via

$$c^0_i = c^N_i \qquad c^{-1}_i = c^{N-1}_i \qquad c^{N+1}_i = c^1_i \qquad c^{N+2}_i = c^2_i \tag{38}$$

where $N_x = N_y = N$.

3.1.2 Runge-Kutta methods

Now that the PDE in question has been discretized into a system of ODEs we can solve it with the help of time integration methods. A very commonly used method is the family of Runge-Kutta methods. We begin with the *Euler method* and consider a general system of ODEs solved by a vectorial function $\mathbf{c}(t)$:

$$\frac{\partial \mathbf{c}}{\partial t} = \mathbf{f}(\mathbf{c}(t), t)\ . \tag{39}$$

We approximate the left side with

$$\frac{\partial \mathbf{c}}{\partial t} \approx \frac{\mathbf{c}(t + \Delta t) - \mathbf{c}(t)}{\Delta t} \tag{40}$$

and solve for $\mathbf{c}(t + \Delta t)$:

$$\mathbf{c}(t + \Delta t) = \mathbf{c}(t) + \Delta t \cdot \mathbf{f}(\mathbf{c}(t), t). \tag{41}$$

If the time t is discretized by $t_i = t_0 + i\Delta t$ with time step Δt, the solution $\mathbf{c}$ is also discretized as c_i.

$$\mathbf{c}_{i+1} = \mathbf{c}(t_{i+1}) = \mathbf{c}_i + \Delta t \cdot \mathbf{f}(\mathbf{c}(t_i), t_i) \tag{42}$$

This is the Euler method. The system of ODEs is solved with an initial condition $c_0 = c(t_0)$ iteratively for each time step. Whichever term is multiplied with the time step determines the *Runge-Kutta method* that is given by

$$\mathbf{c}_{i+1} = \mathbf{c}_i + \Delta t \cdot \sum_{j=1}^{n} q_j \mathbf{k}_j \tag{43}$$

for the n'th stage, with

$$\mathbf{k}_j = \mathbf{f}\left(t_i + \alpha_j \Delta t, \mathbf{c}_i + \Delta t \sum_{l=1}^{j-1} \beta_{jl} k_l\right). \tag{44}$$

q_j, α_j and β_{jl} are coefficients that classify the Runge-Kutta method further. They are usually listed in *Butcher tablaus* [But08].

3.1.3 Final implementation

The 1D simulations are done with a self-written python code which implements abovementioned methods. The time integration is done via the Runge-Kutta Fehlberg[Feh69] method. As for the 2D simulations, they are done with the same code used by Dr. M. Wilczek [Wil12]. It is a CUDA [NVI17] code written in C++ which employs "General Purpose Computation on Graphics Processing Unit" (GPGPU). The used time integration method is Runge-Kutta Dormand-Prince[DP80]. Both, this and Runge-Kutta Fehlberg, are implemented as adaptive stepsize integration algorithms.

4 Simulations in 1D

The main control parameter for LB transfer is the *transfer velocity*. The behavior of the above mentioned model under variation of the velocity has been investigated extensively in previous works [KGFT12, KT14, Wil12, WG14]. In these works studies on the *contact line position* x_s and the *boundary concentration* c_0 have also been done. In the following we will recap some of the results that are known and relevant for this thesis. Furthermore, we will only consider the one-dimensional case where the solutions correspond to profiles of the two-dimensional case which are parallel to the transfer direction.

4.1 Constant transfer velocity

The solution space has been studied in [KGFT12, KT14]. Fig. 9 shows that for a certain range of transfer velocities v, 1D solutions are time-periodic (blue solution branch, label β), representing a pattern of alternating *liquid-condensed* (from now on LC) and *liquid-expanded* (from now on LE) phases moving along the transfer direction. For larger or smaller velocities the solutions become stationary in time (black solution branches). They represent LC (label a and c) and LE phases (label l) respectively. We will call the region of time-periodic solutions the patterning regime from now on. The onset of the patterning regime at low velocities occurs at an unsteady steady state on the snaking part (labels d to j). There, the time-periodic solutions emerge as a result of a *homoclinic bifurcation*. At high velocities the patterning regime ends in a series of *Hopf bifurcations* where the last one is *subcritical*. Note that there actually are more time-periodic branches (unstable) connecting the part of steady states on the right side of the minimal L^2 value to the snaking part (cf. [KT14]).

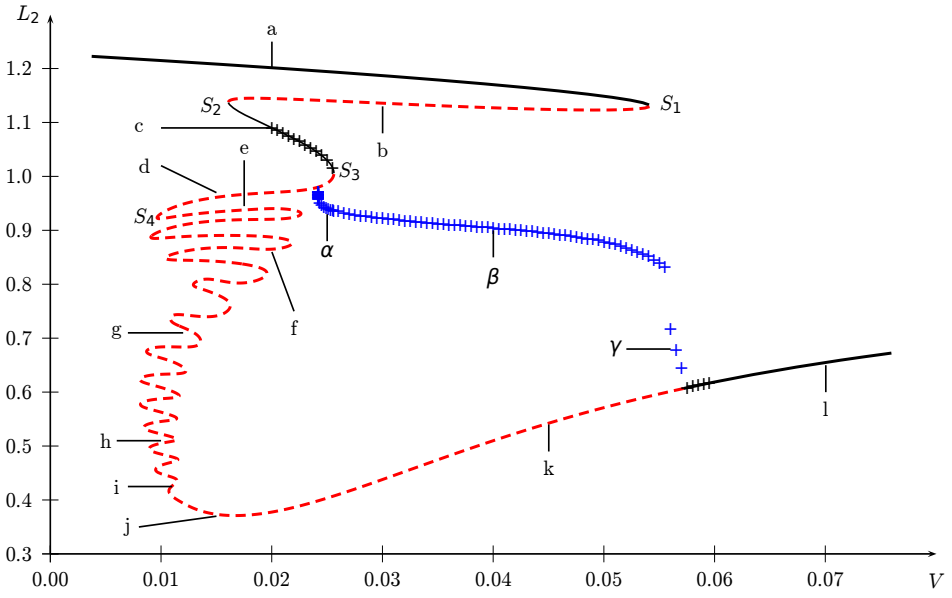

Figure 9: One-dimensional bifurcation diagram for constant transfer velocity v with L^2 norm as solution measure. Solutions along lines were obtained by numerical continuation and crosses by direct numerical simulations. Solid lines correspond to stable solutions. The focus should be on the stable branch of periodic solutions in blue and the stable branches of stationary solutions in black ([KGFT12]).

Examples for these solution types are shown in Fig. 10 .

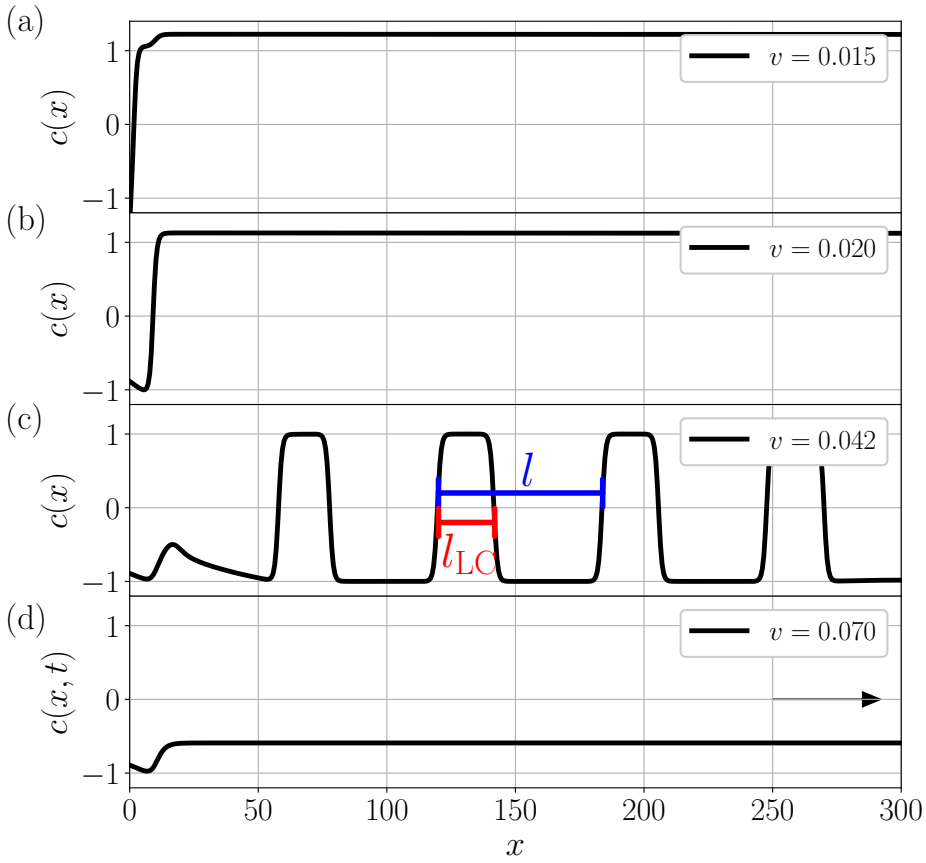

Figure 10: One-dimensional stable solution types for different constant transfer velocities v obtained by numerical integration of Eq. (9). (a,b) LC stationary solutions, corresponding to different LC branches. (c) A snapshot of LC/LE time-periodic solution with *stripe distance* l (blue) and *length of LC phase* l_{LC} (red). (d) LE stationary solution. Transfer direction is denoted by black arrow

There exists a velocity range where bistability between the two LC solutions occurs and also between the solutions on branch a and the time-periodic solutions. Choosing the initial condition as in Eq. (12) (a simple meniscus) mainly leads to the solutions on branches c, β and l. Note that the L^2 norm for the LC and the time-periodic solution decreases with increasing velocity while the norm for the LE solution increases, meaning that the molecule density $c(x,t)$ of the LC solution decreases with increasing v and that of the LE solution increases. As for the time-periodic solutions, the portion of LC phases decreases.

This thesis mainly focuses on the behavior of time-periodic solutions. Thus, besides the L^2 norm, three more solution measures are used depending on the context and usefulness. One is the as in Fig. 10 (c) defined *stripe distance* l. In the 1D case stripe distance l is the distance between two subsequent falling (or rising) flanks while l_{LC} is the *length of* the *LC phase* of one stripe (cf. Fig. 10). The second measure is the in Sec 2.2 defined *synchronization order* W (cf. Eq. (19)) and the last one is the *duty cycle* D

$$D = \frac{l_{LC}}{l} \,. \tag{45}$$

In Sec. 5 we will investigate the 2D system. There, the periodic solutions mostly form stripe patterns. Which means that $c(x,y,t)$ is constant in one direction and periodic in the other. This is why the term stripe distance is already used here for the 1D system. Another reason for the choice of this measure is that there will also be periodic solutions with varying

distances between subsequent stripes. In that case the wavelength λ is usually not the same as stripe distance l.
Choosing l as the solution measure, the branch of periodic solutions in Fig. 9 is shown in Fig. 11.

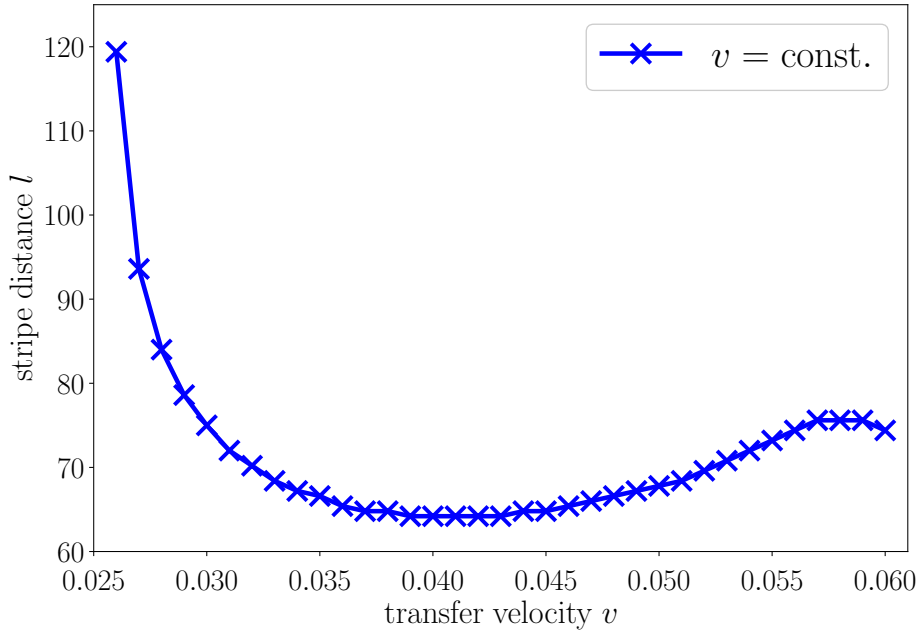

Figure 11: Dependence of stripe distance l of 1D time-periodic solutions on transfer velocity v, obtained from numerical integration of Eq. (9).

One can see that l does not depend monotonically on v. Starting from the local minimum, l increases until $v \approx 0.0256$ and also in the other direction until $v \approx 0.060$. l actually keeps on increasing until the periodic solution transitions to LE solutions for higher velocities (cf. [Wil12]). The calculations just need to be done more carefully by moving along the solution branch. The behavior can be understood intuitively for the LB-transfer because for low transfer velocities there is enough time to supply surfactants from the water surface to the substrate through convection flow and capillary force. Therefore the portion and spatial length of LC phase within the stripe solution increases with decreasing velocity. For high velocities the surfactants are not supplied fast enough and the portion of LE phase increases. Near the end of the patterning regime at $v \approx 0.060$ the location at which the stripes emerge in space shifts away from the contact line with increasing transfer velocity. Upon reaching the last Hopf bifurcation the formation of stripes stops, resulting in a LE solution [KGFT12]. This is a behavior we will find for time-periodic transfer velocity as well.

4.2 Transfer onto prestructured substrates

One advantage in LB-transfer is being able to control small scaled patterns on large scales. One way to accomplish that is by introducing spatial forcing, e.g. by the means of prestructures (cf. [Wil12, Wil16]). This is done by introducing spatial modulations to the SMC field $\zeta(x,t)$. It locks the spatial frequency of the periodic solutions onto the wavelength of the spatial forcing. This means that the ratio between those two quantities is rational. An example is shown in Fig. 12 where the black line denotes the time-periodic solution and the blue line the SMC field.

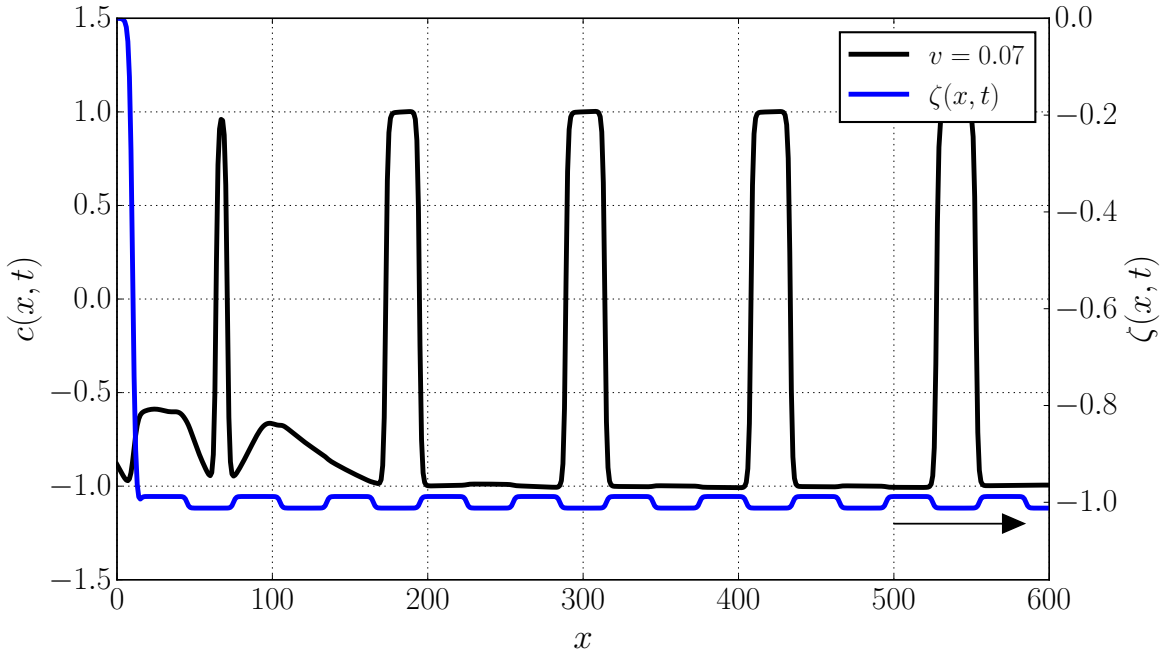

Figure 12: Snapshot of 1D time-periodic solution which exhibits 1:2 synchronization with spatial prestructure periodicity $L_{\text{pre}} = 60$. Obtained from numerical integration of Eq. (9)

.

We see so-called 1:2 synchronization. The spatial frequency of the solution is half of that of the spatial forcing. Or equivalently, the stripe distance is double the spatial periodicity of the prestructure. One might think that creating stripes with the help of a striped prestructure is paradox since the striped prestructure must have been created artifically, therefore the method for creating such stripes already exists and works. However, one aim of LB transfer is to create structures that are as small as possible for large areas while also being able to control their formation. So cases like 2:1 synchronization where the stripe distance is a fraction of the wavelength of the prestructure are certainly desired.

4.3 Time-periodic transfer velocity

Since spatial forcing shows many phenomena that appear in synchronization, it is only natural to investigate the system with temporal forcing. In addition, changing the transfer velocity in time does not require prior modification of the substrate as with prestructures. For this aim, we modulate the transfer velocity with a sine function with amplitude A, mean velocity v_0 and angular frequency (from now on shortened to frequency) ω.

$$v(t) = v_0(1 + A\sin(\omega t)) \tag{46}$$

As a result from the forcing term time-periodic solutions can have multiple different periods and stripe distances. Therefore, we introduce the mean (in time) stripe distance l_0 which is one of the relevant quantities when we investigate synchronization effects.

4.3.1 v_0-scan

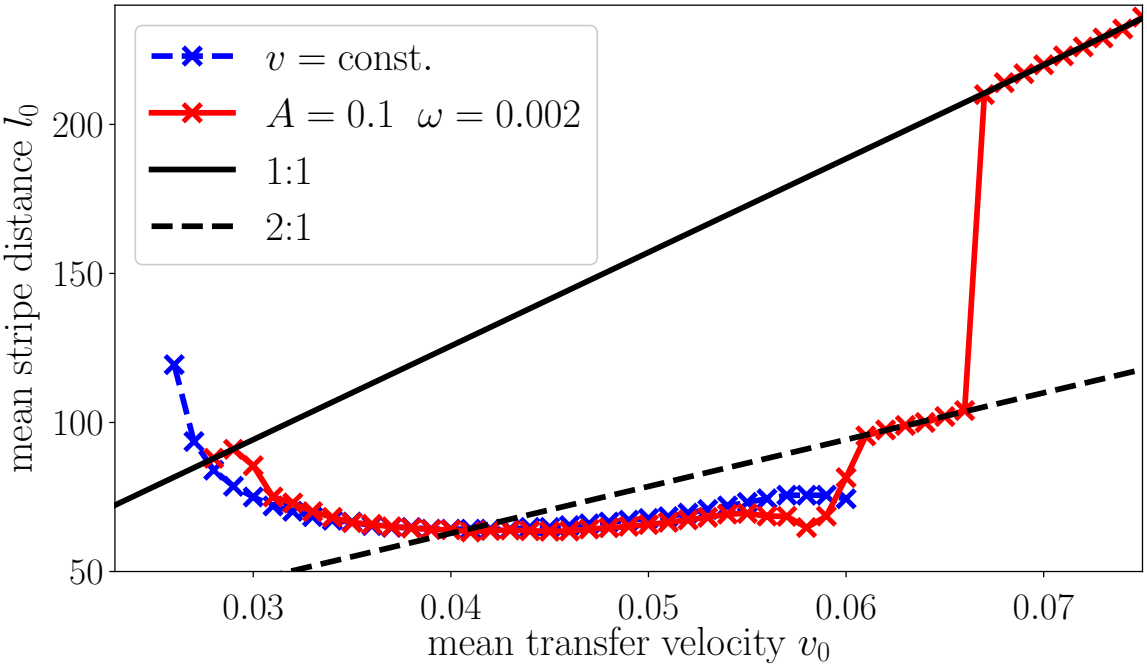

Figure 13: Dependence of mean stripe distance l_0 on mean transfer velocity v_0 in the case of time-periodic forcing with $A = 0.1$, $\omega = 0.002$ (red) and in the case of constant transfer velocity(blue). The 1:1 and 2:1 synchronization lines (black) are drawn in aswell.

Figure 13 shows the dependence of l_0 on v_0 together with the data for constant transfer velocity (blue). We observe that the forcing data deviates from the unforced ones towards the end of the patterning regime. Furthermore, the parameter range of time-periodic solutions is extended in the direction of high velocities. There, at $v_0 = 0.058$, l_0 exhibits a dip to lower values before increasing again in order to transition into linear behavior. This linear dependence of l_0 on v_0 represents the occurance of synchronization. For that it is useful to derive or motivate an equation that relates the spatial distance l between stripes of time-periodic solutions and the forcing term.

As mentioned in Sec. 2.2 synchronization through external forcing leads to locking of the mean frequency Ω_0 of the system that is being forced onto the forcing frequency ω. In our case

$$\Omega_0 = \frac{2\pi}{\tau_0} \tag{47}$$

is defined such that τ is the time it takes for the solution to advect by one full stripe. Or, in other words, the time difference between arrival of one falling flank at one point in the domain until arrival of the next falling flank. Here, τ_0 is its mean value over time.

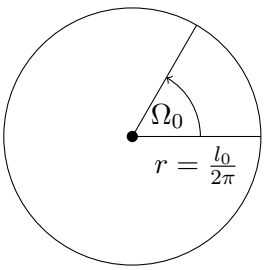

Figure 14: Circular motion with angular frequency Ω_0 and circumference l_0

If one considers a solution with mean frequency Ω_0, then the stripes also move with mean velocity v_0. Consequently it is possible to map the time-periodic solutions onto a point moving on a circle with constant frequency Ω_0. And since after one rotation the solution will have advected by one mean stripe distance l_0 on average, we choose the radius r such that $2\pi \cdot r = l_0$. Using the known relation $v_0 = \Omega_0 \cdot r$ for circular motion with constant frequency and eliminating r, we arrive at

$$l_0 = \frac{2\pi}{\Omega_0} v_0 \ . \tag{48}$$

Lastly, we insert the definition of synchronization order $W = \frac{\Omega_0}{\omega}$ for

$$l_0 = \frac{2\pi}{\omega W} v_0 =: \frac{l_f}{W} \ . \tag{49}$$

l_f is the stripe distance which is forced for 1:1 synchronization. This equation will be frequently used to determine synchronization regions.
Note that, l_0 depends inversely on ω and W and linearly on v_0.
Using Eq. (49) with the used parameters and the mean stripe distance we find the two linear functions that pass through the two sets of linear data. Hence, for $A = 0.1$ and $\omega = 0.002$ the time-periodic solutions show visible regions of 2:1 and 1:1 synchronization. Fig. 15 shows the time evolution of l for the case of 2:1 synchronization. The solution exhibits two stripe distances that alternate between each other. The mean frequency of their occurrence is double the forcing frequency ω. This can be visualized by the second return map where each measured stripe distance l_{n+2} is drawn against l_n. Both points lie on the angle bisector, showing that the stripe distance is in indeed two-periodic.

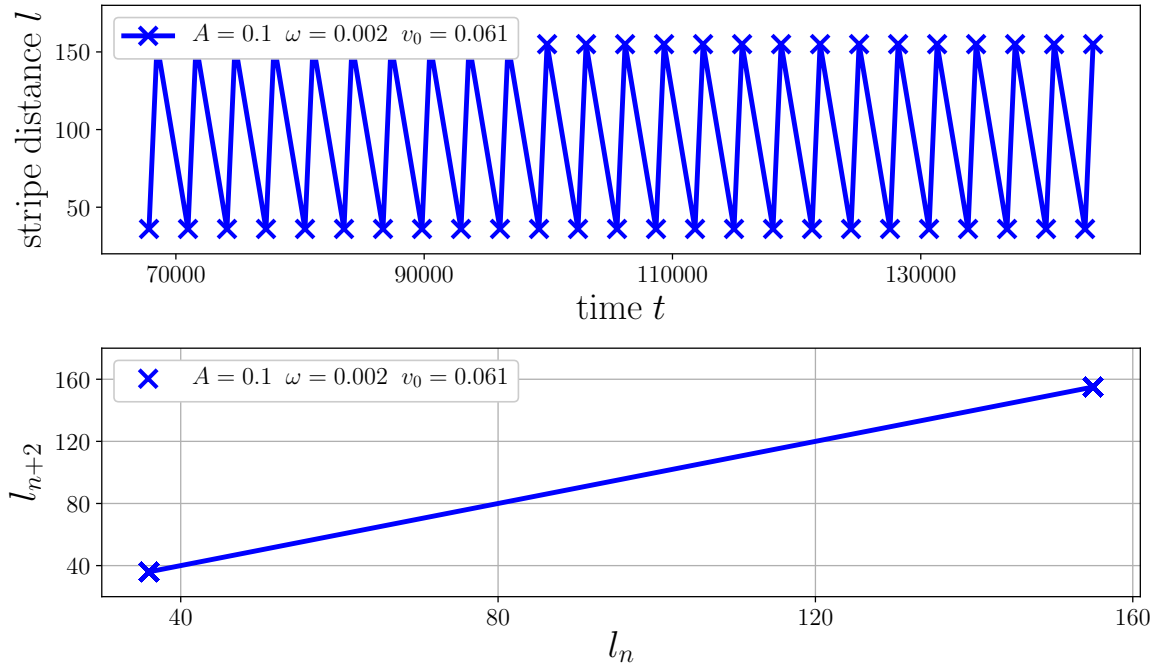

Figure 15: Top: Time evolution of stripe distance l calculated for $A = 0.1$, $\omega = 0.002$, $v_0 = 0.061$. Bottom: second return map of stripe distance l_n, indicating its two-periodic behavior.

For the system in Eq. (9) the stripe distances $l_{\text{const.}}$ of the constant transfer case represent the natural stripe distances of the system. The occurance of synchronization not only depends on the amplitude A but also on the difference between $l_{\text{const.}}$ and the stripe distance that is imposed by the forcing (analogously to the frequency difference, cf. Sec. 2.2). The higher the amplitude the larger the region of synchronization and the lower the synchronization orders become.
In our case the solutions for $v_0 \in (0.029, 0.031) \cup (0.057, 0.061)$ show higher synchronization orders like 14:5 for $v_0 = 0.058$. However, for $v_0 \in [0.031, 0.057] \setminus \{\sim 0.041\}$ the difference between natural and imposed stripe distance is too large so the system does not show low

order synchronization. Instead it locks onto even higher synchronization orders where the imposed stripe distances are close to $l_{\text{const.}}$ and therefore the amplitude requirement for locking is lower. For $v_0 \gtrsim 0.060$ the range of periodic solutions for $v = \text{const.}$ ends, which facilitates the locking of solution frequency onto the forcing.
For more clarity we introduce the above mentioned, missing solution measure: the synchronization order W. Figure 13 then transforms to Fig. 16.

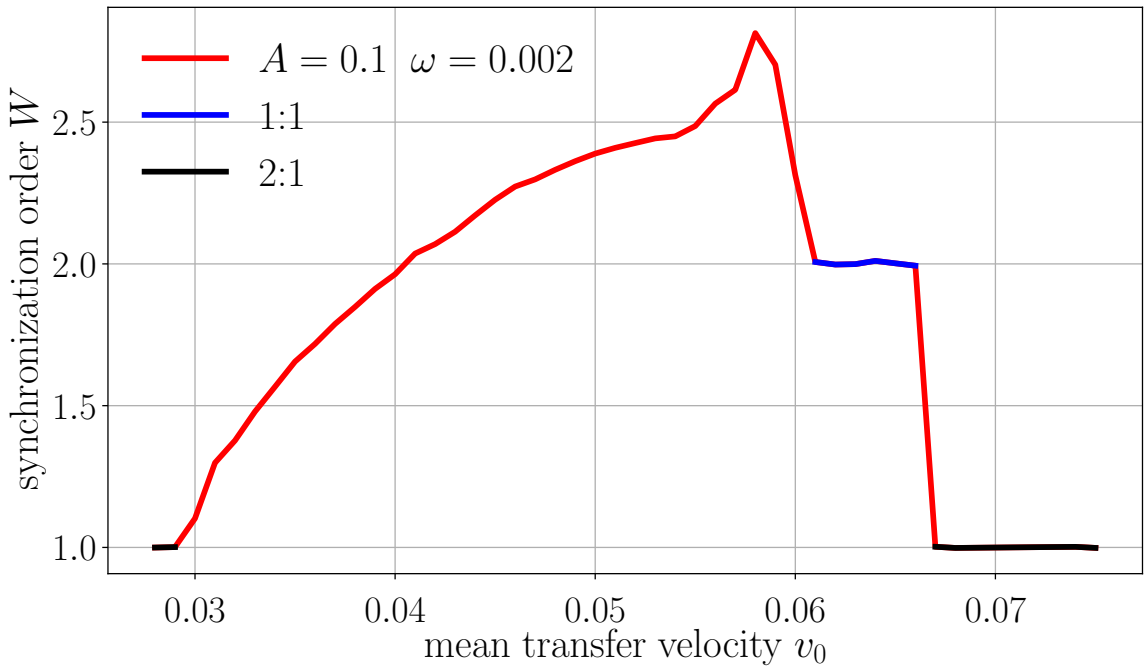

Figure 16: Dependence of synchronization order W on mean transfer velocity v_0 in the case of time-periodic forcing with $A = 0.1$, $\omega = 0.002$. The 1:1 and 2:1 synchronization plateaus are drawn as well.

Here, plateaus represent larger regions of synchronization. The slight deviations from actual plateaus are consequences of the spatial discretization, resulting in errors for the measurement of l_0.

4.3.2 ω-scan

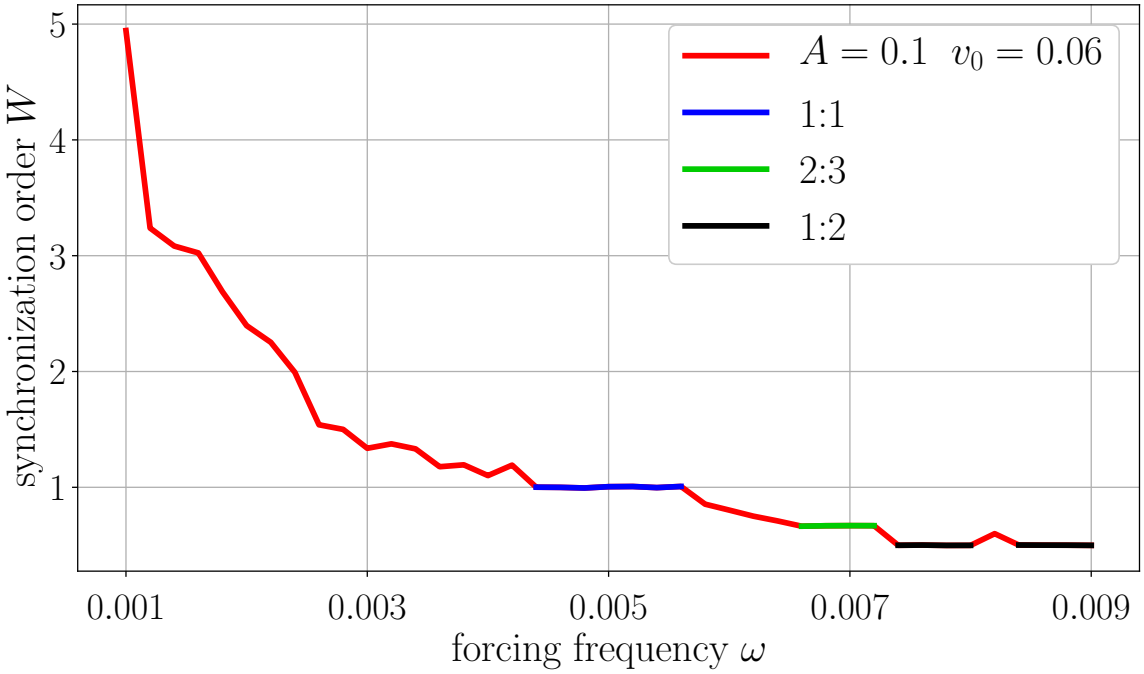

Figure 17: Devil's staircase obtained by calculating the dependence of synchronization order W on forcing frequency ω with $A = 0.1$, $v_0 = 0.060$. The occuring synchronization plateaus are marked as well. 1:1(blue), 2:3(green), 1:2(black).

Figure 17 shows the dependence of W on ω for $A = 0.1$, $v_0 = 0.060$. It shows an almost monotonically decreasing W. This is precisely a devil's staircase, as introduced in Sec. 2.2. Larger occurring plateaus correspond to 1:1, 2:3 and 1:2 synchronization, also indicating the tendency for larger plateaus when W is formed by small integer values.
Looking back at Fig. 11, $v_{\text{const.}} = 0.060$ can be identified with $l_{\text{const.}} = 74.4$ which is about the forced stripe distance of $\omega = 0.0051$. Since the natural stripe distance $l_{\text{const.}}$ of the system stays the same as long as v is not changed, we expect synchronization regions to appear relatively close to $l_{\text{const.}}$ which is the case as can be seen in Fig. 18. Upon switching synchronization order the change in l_0 is not as significant as for the scan in v_0 (cf. Fig. 13). The odd one out solution at $\omega = 0.0082$ is actually a 3:5 synchronized solution.
In order to further clarify the nature of synchronization a snapshot of a time-periodic solution for parameter set $A = 0.1$, $\omega = 0.007$, $v_0 = 0.06$ is shown in Fig. 19. Looking at Fig. 17 one can see that the parameters lead to a 2:3 synchronized solution. In fact the stripe distance is four-periodic. Their total length corresponds to six times the forced stripe distance l_f determined by Eq. (49). This verifies the 2:3 synchronization.

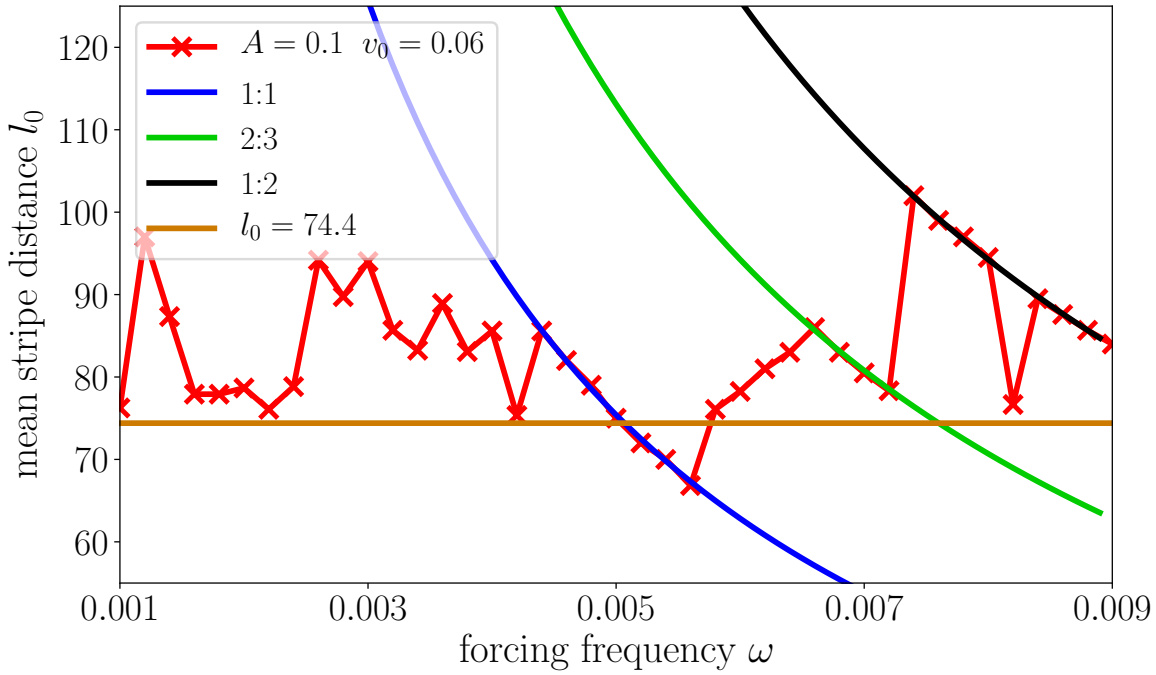

Figure 18: Dependence of mean stripe distance l_0 on forcing frequency ω with 1:1(blue), 2:3(green), 1:2(black) synchronization regions corresponding to the inverse behavior predicted by Eq. (49). The straight line (orange) corresponds to the natural stripe distance originating from the unforced system with transfer velocity $v = 0.06$.

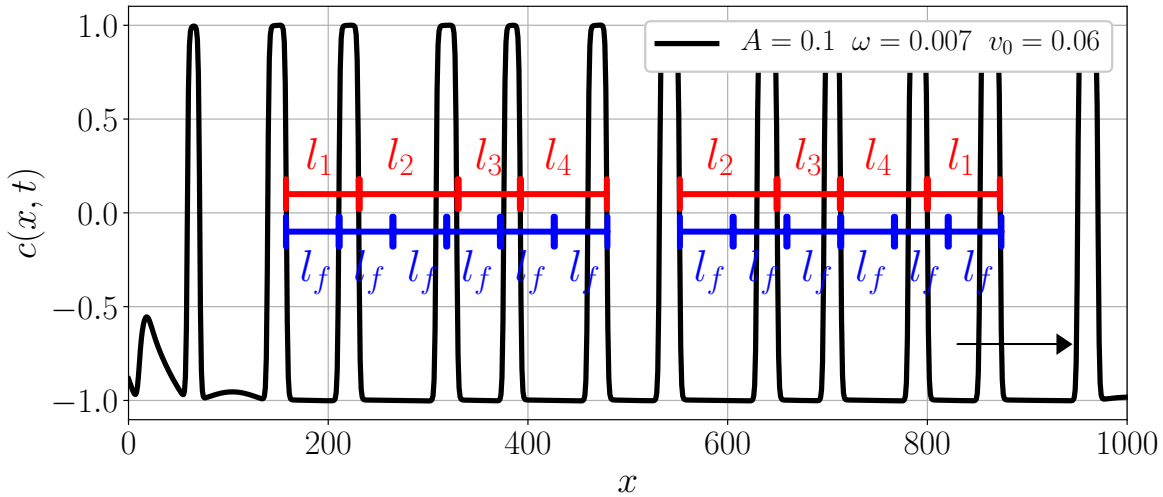

Figure 19: Snapshot of time-periodic solution for $A = 0.1$, $\omega = 0.007$, $v_0 = 0.06$. The solution exhibits 2:3 synchronization with 4 different l_i. Forced stripe distance l_f is denoted by blue segments.

4.3.3 v_0-ω-scan

After studying the behavior of the system (Eq. (9)) separately in the v_0 and ω directions in parameter space we investigate it once again while varying both parameters simultaneously. Since the full data set might be confusing at first glance, the parameter space is gradually built up and shown from different perspectives in Fig. 20 - 25. The measured stripe distances can reach lengths of $l = 500$ or more. Thus, the domain needs to be chosen especially large for small ω and high v_0 reaching maximum domain sizes of $L = 5000$ in order to accommodate the stripes and give them enough time to develop and converge within the domain. In order to keep the same discretization the number of grid points is also increased to a maximum of $N = 5000$.
Starting with Fig. 20, the dependence of W on v_0 for $A = 0.1$, $\omega = 0.002$ is shown just like in Fig. 16 but now in v_0-ω-space.

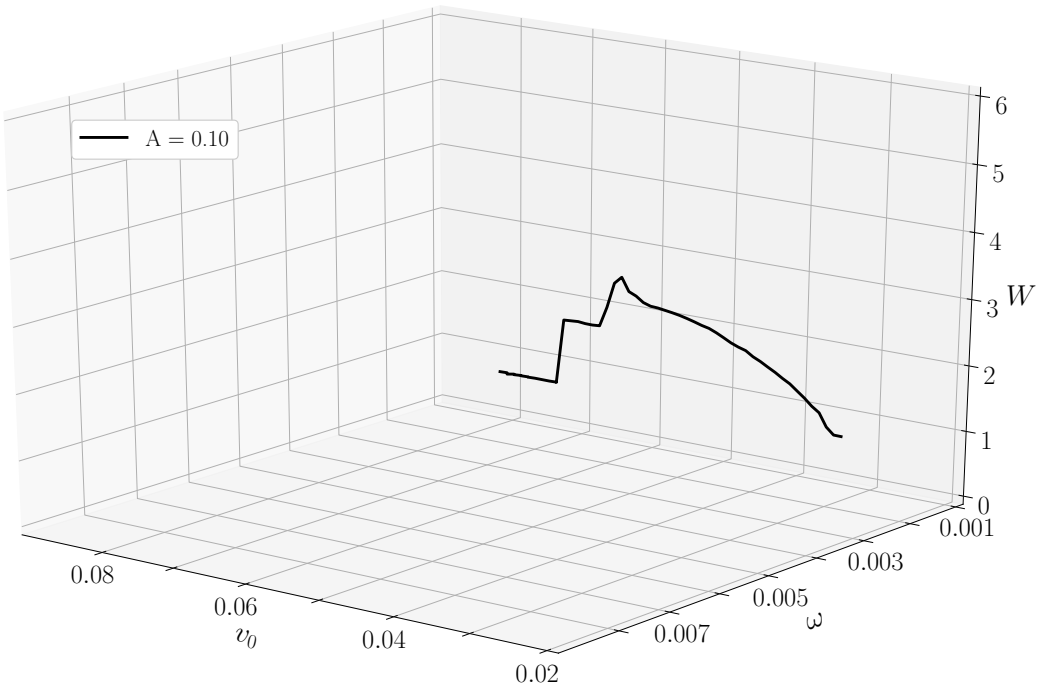

Figure 20: Dependence of synchronization order W on v_0 and ω calculated for $A = 0.1$. Only the data set for $A = 0.1$ and $\omega = 0.002$ is shown (cf. Fig. 16).

Extending the scan to $\omega \in [0.001, 0.009]$ we obtain Fig. 21 where several observations can be made. First of all the periodic solutions only occur within the shown v_0-ranges. Outside of those, just like before, the solutions become stationary. Furthermore, just like before, the patterning regime is extended towards higher velocities but shortened towards lower velocities. Further, there are multiple plateaus which indicate synchronization regions. And thirdly the plateaus are mostly outside or around the limits of the original finally regime $v_0 \in [0.0256, 0.060]$ with constant transfer velocity.

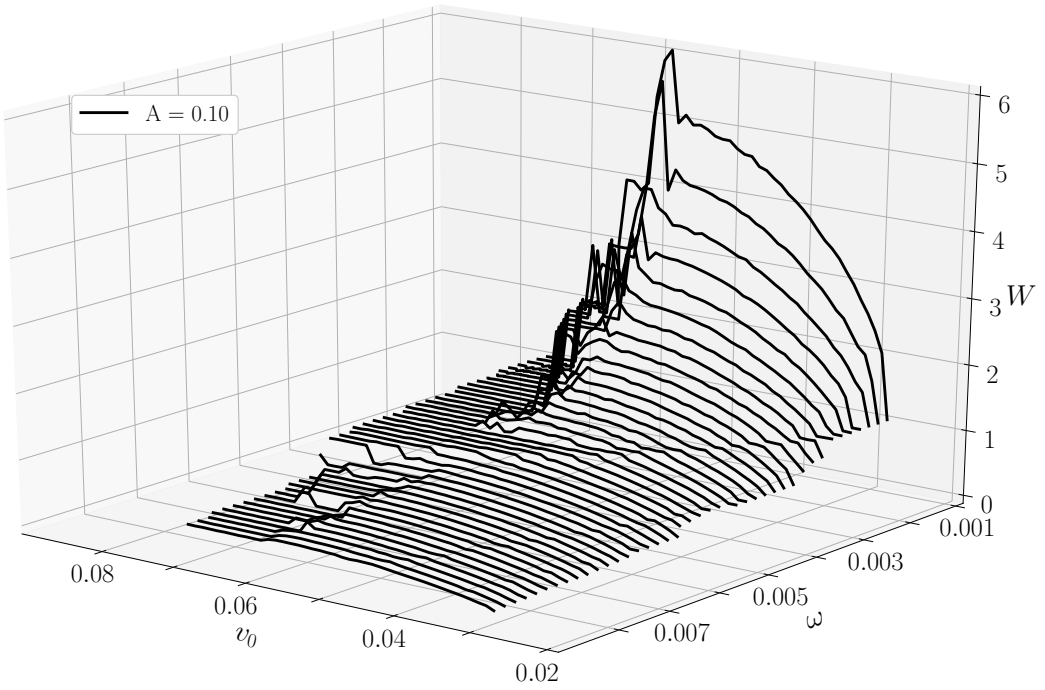

Figure 21: Dependence of synchronization order W on v_0 and ω with $A = 0.1$ for $\omega \in [0.001, 0.009]$. The solutions transition to stationary ones outside of the patterning regime.

Inside that velocity range W becomes especially large for small ω which is something expected for the whole parameter space since W should follow a devil's staircase for each fixed v_0. This can be seen when looking at the ω dependence only (cf. Fig. 22).

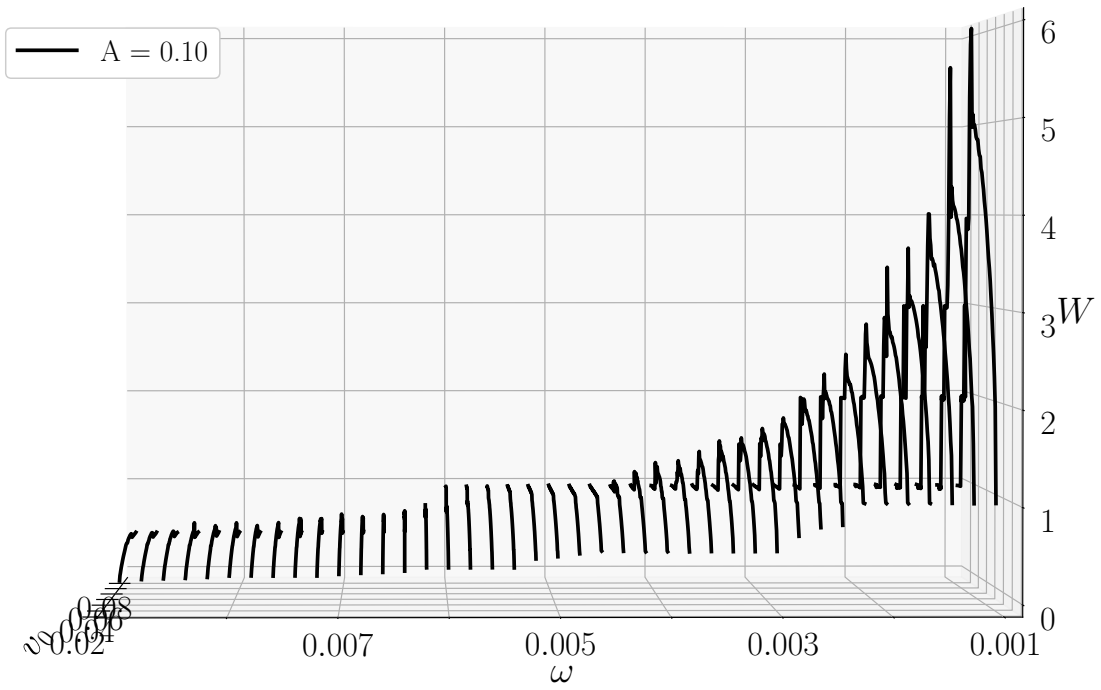

Figure 22: Side view of v_0 - ω - parameter scan shown in Fig. 21 $A = 0.1$. One can see the monotonous decrease of the synchronization order W with increasing forcing frequency ω with occasional plateaus. This is a Devil's staircase as described in Sec. 2.2.

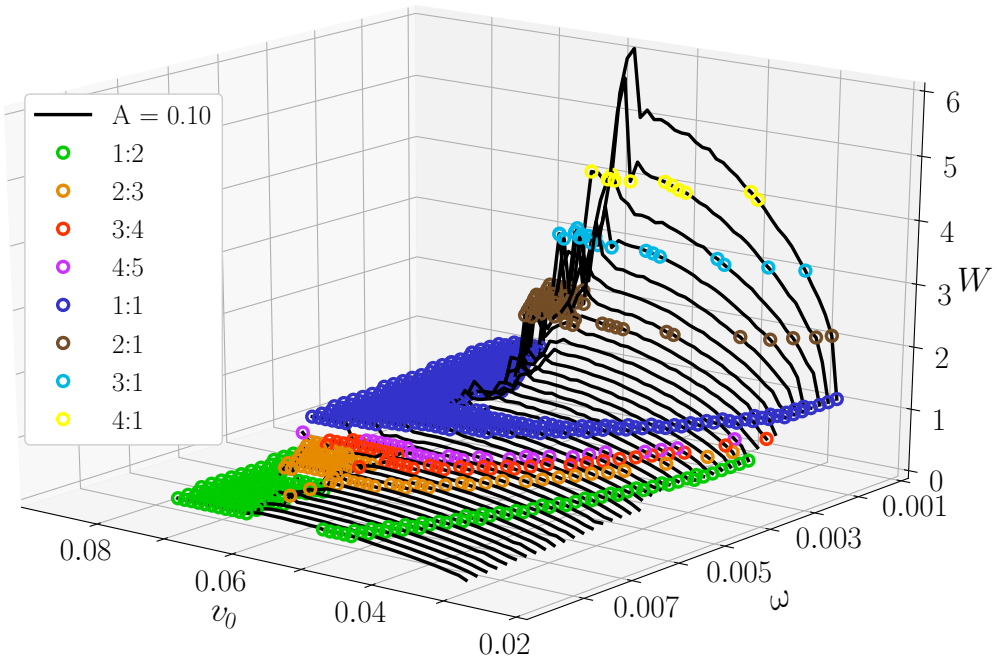

Figure 23: Dependence of synchronization order W on v_0 and ω with $A = 0.1$ for $\omega \in [0.001, 0.009]$. Larger synchronization regions are denoted by different colors.

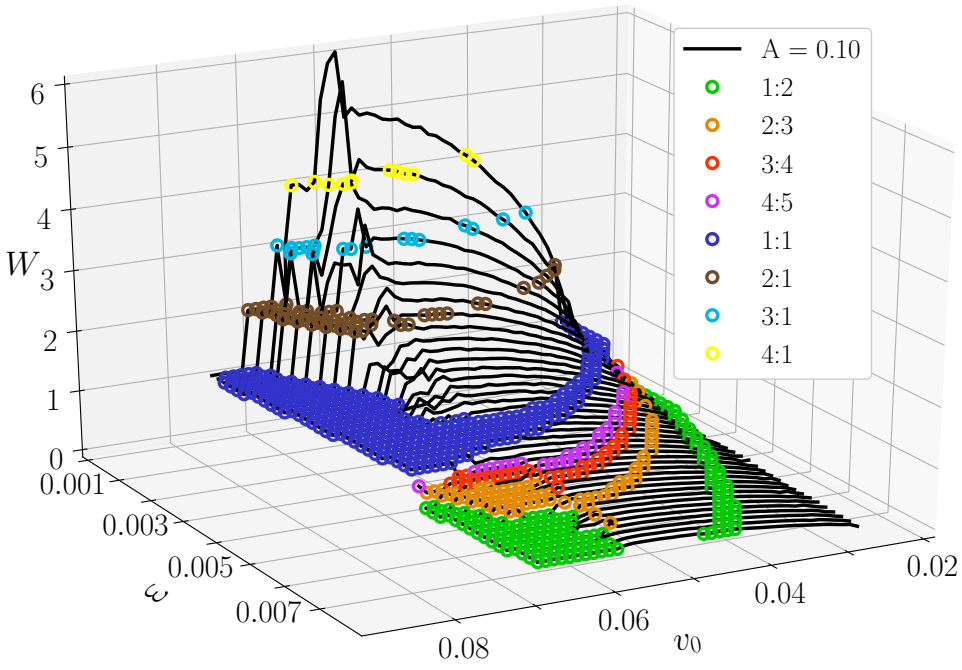

Figure 24: Dependence of synchronization order W on v_0 and ω with $A = 0.1$ for $\omega \in [0.001, 0.009]$ (cf. Fig. 23). Larger synchronization regions are denoted by different colors. Different view angle.

Adding colors for the synchronization orders that occupy larger regions the structure of solution space becomes clearer in Fig. 23 and 24. Though for the purpose of the following discussion a top down view as in Fig. 25 is more useful.

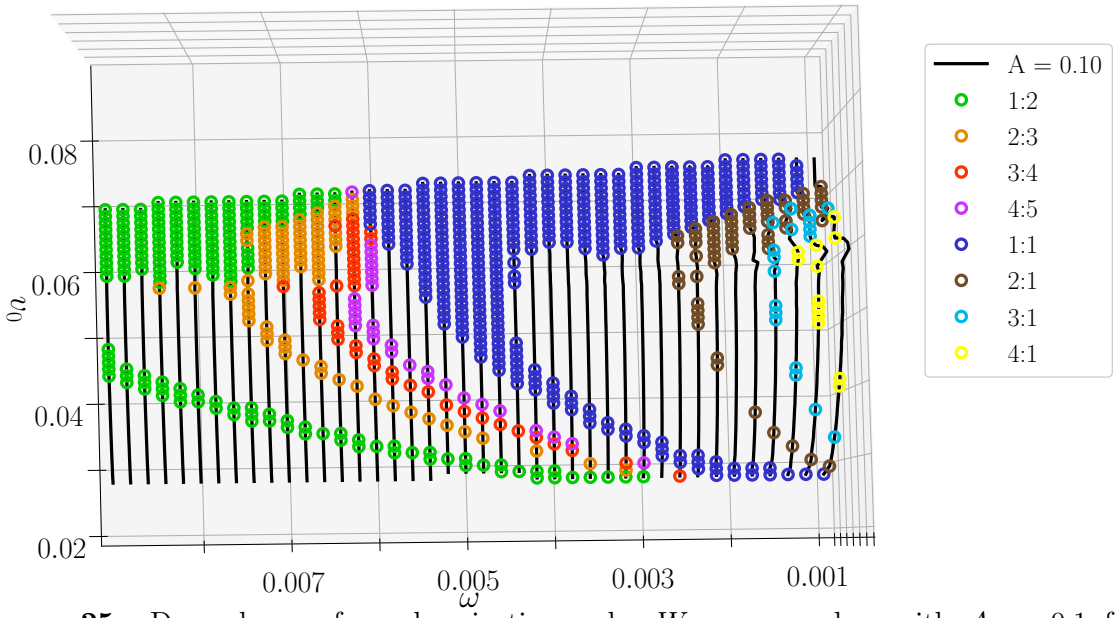

Figure 25: Dependence of synchronization order W on v_0 and ω with $A = 0.1$ for $\omega \in [0.001, 0.009]$. Larger synchronization regions are denoted by different colors. Top down view.

The synchronization orders range from 1:2 to 4:1 while $W = 1$ and $W = 0.5$ occupy the largest regions. The uncolored areas mostly lie within the range of the original patterning regime. As mentioned in previous sections the stripes lock onto stripe distances l_0 close to the natural stripe distance $l_{\text{const.}}$, therefore attaining W's that are composed of higher integer values. Their extent in parameter space is smaller due to that. Of course there are cases where $l_{\text{const.}}$ is close enough to a forced stripe distance with W that consists of low integer value, e.g. at low velocity ranges where $W < 1$. And since the system exhibits 1:1 synchronization around $\omega = 0.005$ it is not surprising for it to exhibit 2:1 and higher multiple synchronization at $\omega = 0.0025$ and lower.
A parameter that has not been changed yet is the amplitude A. And as expected, increasing A leads to larger synchronization regions, especially for low integer W (see. Fig. 26).

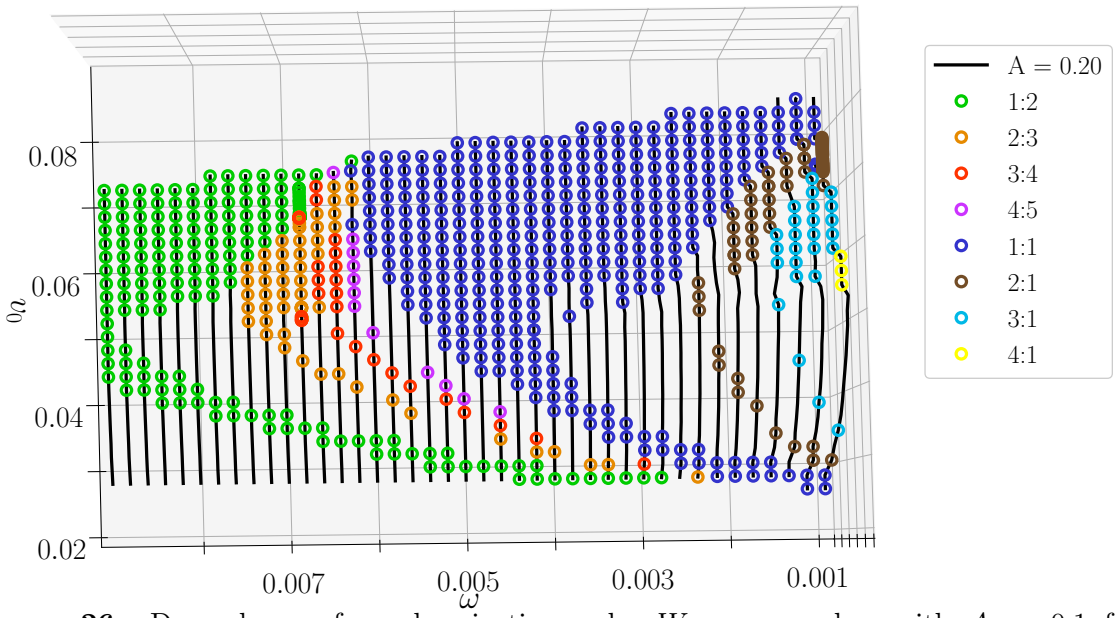

Figure 26: Dependence of synchronization order W on v_0 and ω with $A = 0.1$ for $\omega \in [0.001, 0.009]$. Larger synchronization regions are denoted by different colors. Top down view.

This leads to the in Sec. 2.2 mentioned Arnold tongues.

4.3.4 Arnold tongues

As one can see in Fig. 26, the system (Eq. (9)) shows synchronization orders from 1:1 to 4:1 for $\omega = 0.0014$ and varying v_0. Investigating the behavior of the periodic solutions for varying A corresponds to a scan in a third direction in parameter space. Figure 27 shows the largest regions of synchronization in dependence of A and v_0 with fixed $\omega = 0.0014$. At $A = 0$ the system naturally is not in a synchronized state since A is the coupling constant of the forcing. Regions of low integer ratios like 1:1, 2:1 and 3:1 grow with increasing A whereas the initially existing region of 4:1 is replaced by 3:1 synchronization. So the plot shows the typical shape of Arnold tongues.
The system occasionally takes on different W than in the surrounding parameter space, e.g. for $v_0 = 0.069$ $A = 0.20$. In this case the forced stripe distance imposed by $W = 3$ is a lot closer to the natural stripe distance of the system than the one imposed by $W = 2$. At this point we want to emphasize that the unmarked spaces in the plot still represent synchronized time-periodic solutions. It was just decided not to plot all synchronization orders. This, together with discretized parameter steps is one of the reasons why the 5:2 region seems discontinuous. Though to the right of the 1:1 synchronization region at high v_0 the system does transition to stationary solutions and analogously to the left of the 1:1 region at low v_0. One last observation can be made for $v_0 \in [0.053, 0.065]$. Originally the periodic solutions exist until $v \gtrsim 0.06$ in the unforced system. The forcing extends the region of 3:1 or 2:1 synchronization into the range where stable periodic solutions originally still existed. In this range the synchronization orders change quite rapidly.

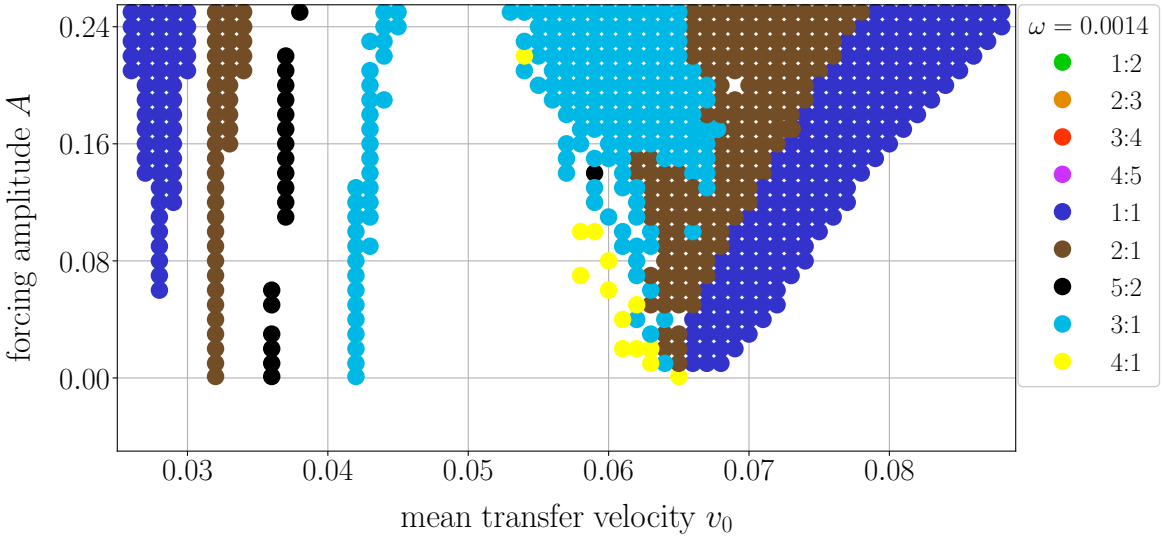

Figure 27: Largest synchronization regions depending on A and v_0 with fixed $\omega = 0.0014$. The regions are denoted by different colors. The plot greatly resembles Arnold tongues introduced in Sec. 2.2

Arnold tongues can also be found for constant v_0 and varying ω, see Fig. 28. Here, the region of time-periodic solutions goes on at the left and right limits of ω. Just like before we observe growth of low integer synchronization regions like 1:1, 1:2 and 3:1. Fig. 26 can also be considered a display of Arnold tongues.

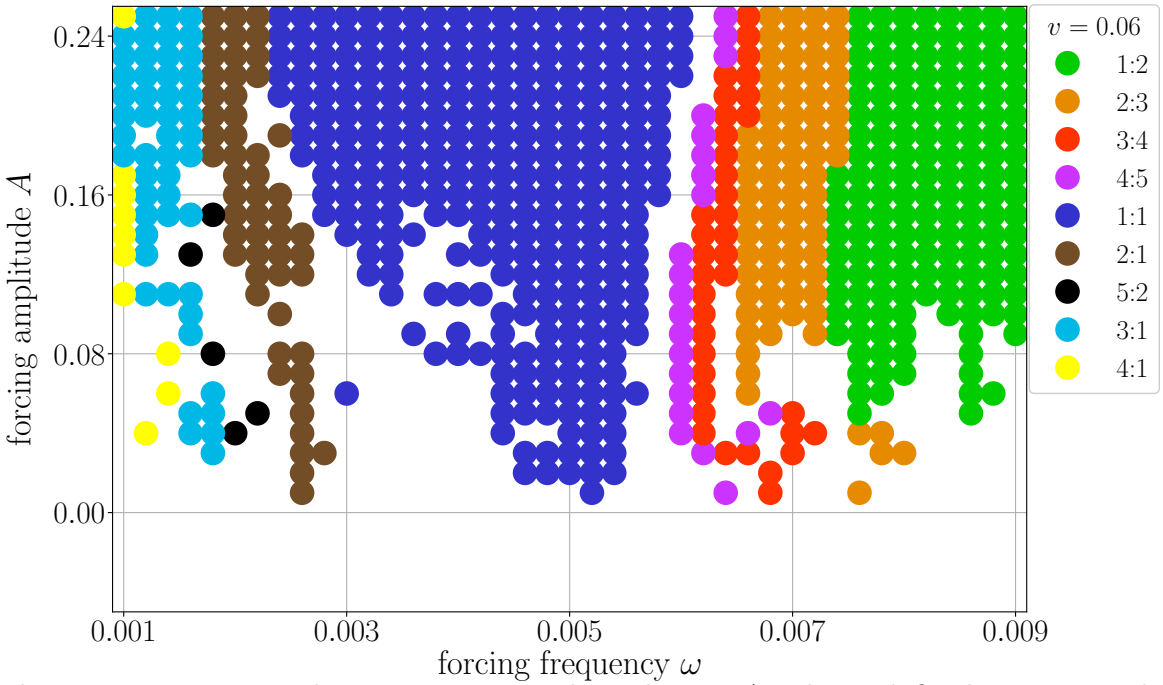

Figure 28: Largest synchronization regions depending on A and ω with fixed $v_0 = 0.06$. The regions are denoted by different colors. The plot greatly resembles Arnold tongues introduced in Sec. 2.2

After these extensive discussions the most important insights can be summarized as follows. First of all, time-periodic forcing (Eq. (46)) leads to synchronization effects, represented by plateaus in W-v_0-ω space and following Eq. (49). These plateaus become larger for low

integer synchronization ratios. Further, the range of time-periodic solutions can be extended outside of the original patterning regime with constant transfer velocity. In addition, synchronization regions can be extended by increasing the forcing amplitude A with synchronization ratios of low integers prevailing over higher ones. Finally, one has to keep in mind that both A and ω affect the stripe distance the system takes on in the end. In contrast to A, ω can cause the system to adapt a high integer value synchronization ratio depending on how close the natural stripe distance / frequency is to ω or its multiples.

4.3.5 Individual stripe behavior

Until now only statements about mean stripe distances l_0 have been made. This section will contain findings about individual stripe distances l_{indi}. For that, we define the individual synchronization order W_{indi}.

$$W_{\text{indi}} = \frac{2\pi}{\omega \cdot l_{\text{indi}}} v_0 \tag{50}$$

In the case of 1:n synchronization, $n \, \epsilon \, \mathbb{N}$, the solutions show no stripe distance variation. Just like in the case of constant transfer velocity the solutions exhibit only one stripe distance as can be seen in the ω-scan presented in Fig. 29. There, W is plotted against ω with $A = 0.2$ and $v_0 = 0.06$. For the synchronization regions 1:1, 1:2 and 1:3, W_{indi} is drawn in as cyan colored circles.

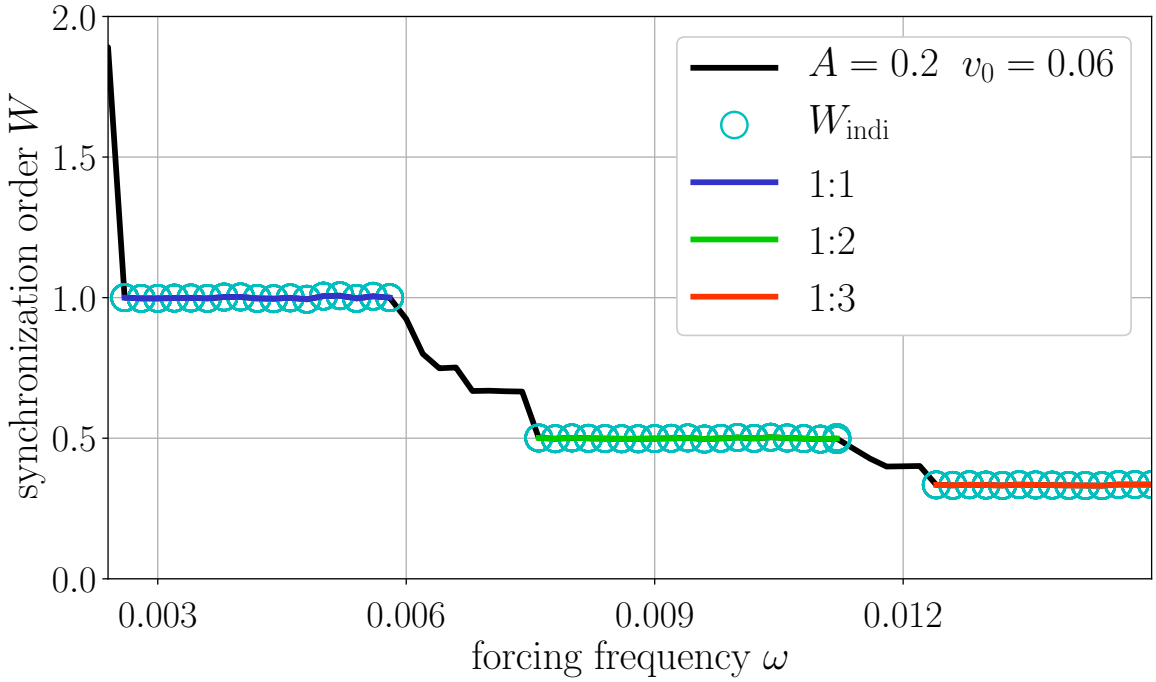

Figure 29: Dependence of synchronization order W on forcing frequency ω with fixed $A = 0.2$, $v_0 = 0.060$. W_{indi} (see Eq. (50)) resulting from individual stripe distances l_{indi} are plotted as cyan rings.

Although 1:n synchronization, $n > 1$, leads to larger stripes than for 1:1 (since the solution frequency is smaller than ω), the fact remains that there usually is no variation of l for these synchronization orders. Unfortunately, that is not always the case. For example, for $A = 0.2$, $\omega = 0.002$ and $v_0 = 0.028$ leads to a 1:1 synchronized solution but with two different l that alternate between each other in time (not shown here).
Figure 30 shows the dependence of the previously defined duty cycle $D = \frac{l_{LC}}{l}$ on ω for $A = 0.2$

and $v_0 = 0.06$. From this, one cannot confidently discern any general behavior. There might be a tendency to adapt to $D \approx 0.25$ starting at $\omega = 0.0026$.

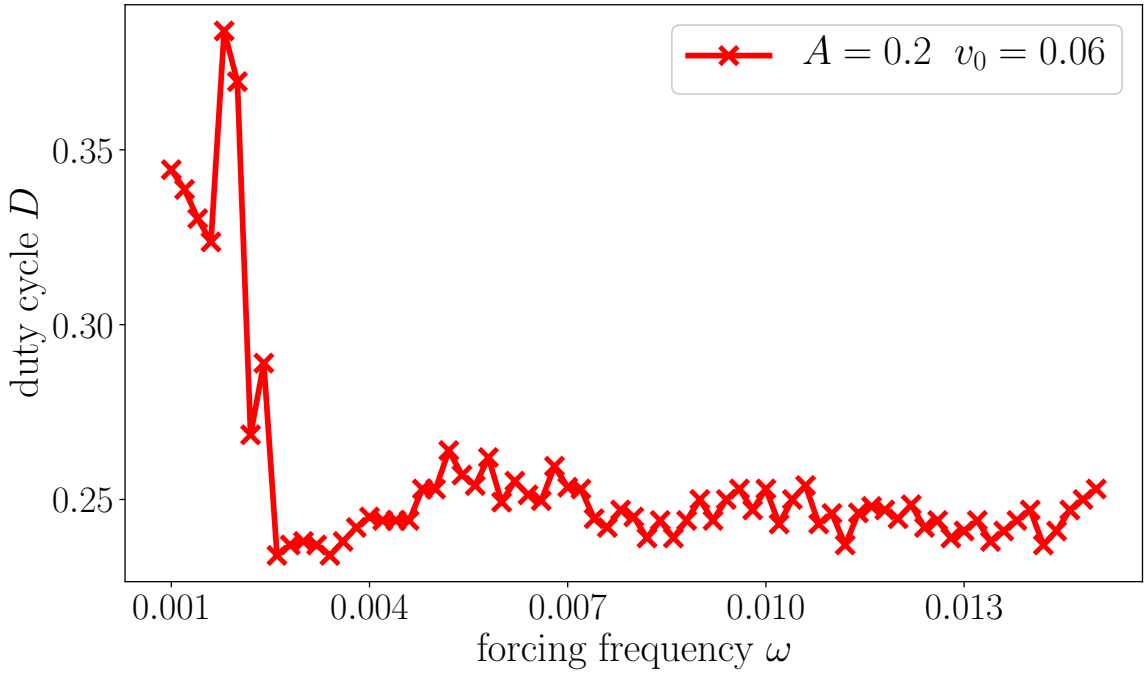

Figure 30: Dependence of duty cycle D on forcing frequency ω with $A = 0.2$, $v_0 = 0.06$. It is not possible to discern any general behavior.

In contrast to that, the behavior of D is simpler for varying v_0. D decreases monotonically with increasing v in the case of constant transfer. With time-periodic forcing, the system follows this natural duty cycle and then shifts when locking onto the forcing with W comprised of low integer values, see Fig. 31.

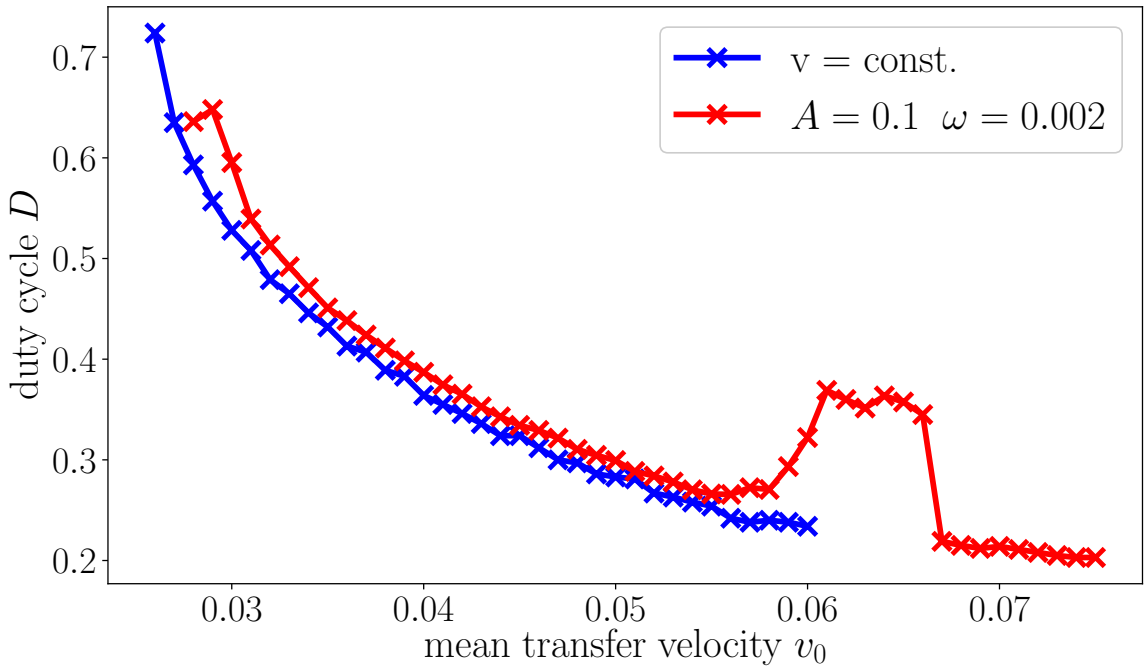

Figure 31: Dependence of D on mean transfer velocity v_0 with $A = 0.1$, $\omega = 0.002$

This inverse behavior can be explained by looking at the definition of D which is $\frac{l_{\mathrm{LC}}}{l}$ and also at Fig. 9 where it was determined that the L^2-norm of time-periodic solutions decreases with increasing v, meaning that the portion of LE phase increases. Concurrently the portion of LC phase decreases. This should still be true for the forced system (Eq. (9),(46)). Additionally, in synchronized regions Eq. (49) gives a linear relationship between l_0 and v_0, thus l_0 grows with increasing v_0. Since l is in the denominator of Eq. (45), linear growth in l leads to inverse decrease in D.

5 Simulations in 2D

The investigation of the 1D system delivered quite a few insights into its behavior, especially regarding synchronization. But it is also necessary to look into the 2D system since that is where actual patterns are possible. In this section the transfer will occur perpendicular to the contact line which means from bottom to top. So the y-direction will be the horizontal and the x-direction the vertical one. This is done in order to see the connection between 1D and 2D solutions more easily. We begin by recapping some known results(cf. [WG14][Wil16]).

5.1 Constant transfer velocity

If one naively extends the 1D solutions along the y-direction, one will expect two spatially homogeneous solutions which represent purely LC and LE phases, excluding the region around the contact line. And the analogous time-periodic solution would be stripes of alternating LC and LE phases which are parallel to the meniscus. Indeed, just like in the 1D case there exists a patterning regime within which time-periodic solutions occur, while outside the system exhibits stationary ones. A striking difference to the 1D system is a transversal instability that occurs for low velocities within the patterning regime. Initial conditions that are inhomogeneous in the y-direction lead to the formation of stripes which extend perpendicular to the contact line. These types of stripes will be classified as vertical and the other ones as horizontal from now on. They can be seen in Fig. 32 for $v_x = 0.026$ and $v_x = 0.04$. The existence of the region of transversal instability has been confirmed via linear stability analysis Wil12.
The vertical stripe solutions have long transient times during which the y-direction wavenumber k_y slowly changes to the one preferred by the system through introducing defects.

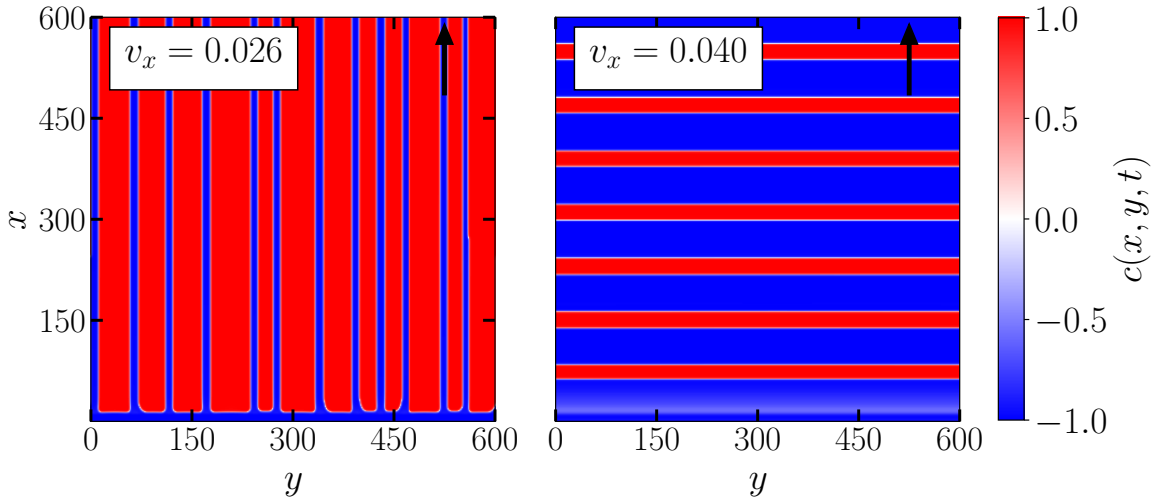

Figure 32: 2D solutions of Eq. (9) with initial condition as in Eq. (12) obtained from direct numerical simulations. Horizontal and vertical stripes for constant transfer velocity $v_x = 0.040$ and $v_x = 0.026$. The transfer direction is denoted by a black arrow.

5.2 Time-periodic transfer velocity

5.2.1 Verification of 1D results

The effects of prestructures have also been investigated for the 2D system and the relevant results will be mentioned at the appropriate points.
We introduce the same forcing term as before, see Eq. (46), and choose a simple meniscus

that is homogeneously extended in the y-direction in order to confirm the results from the 1D simulations. After performing a parameter study in $v_{x,0}$ we find expected results. The mean stripe distance in x-direction $l_{x,0}$ follows the natural one, which is determined by the unforced system, quite closely. The solutions exhibit 1:1 and 1:2 synchronization. In addition, the patterning regime is extended towards higher velocities and the 1:1 synchronization region deeply extends into the original patterning regime. These properties agree with the 1D results (cf. Fig. 33. The extension of the patterning regime occurs with prestructures, too (cf. [Wil16]). A scan in ω_x direction also delivers anticipated results as well, e.g. a devil's staircase (cf. Fig. 34).

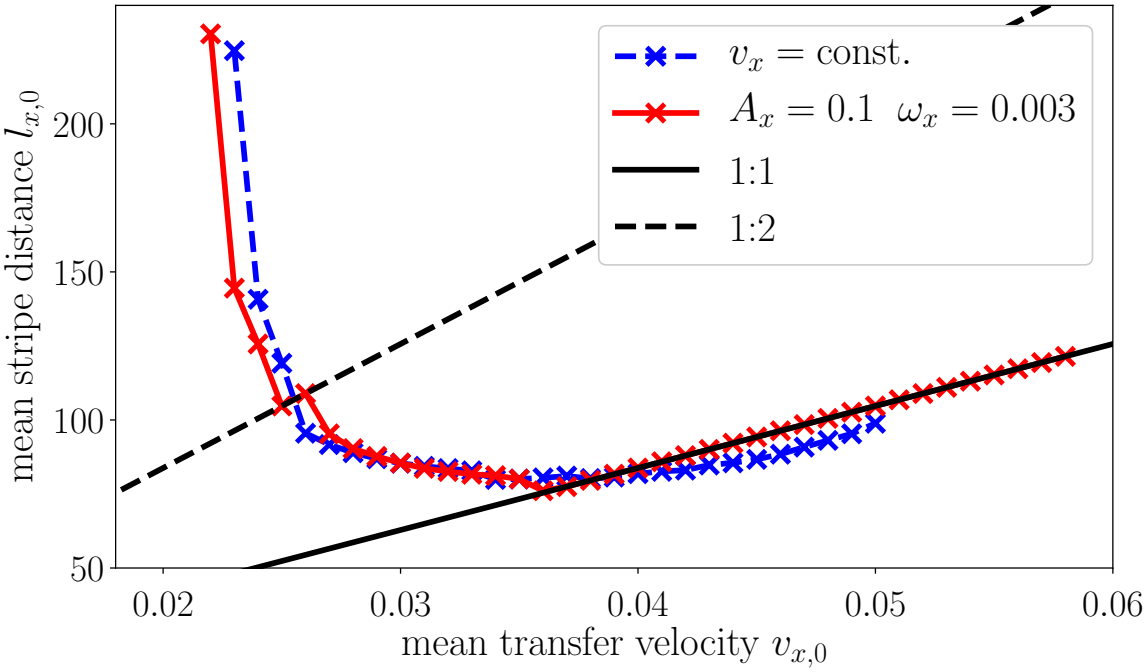

Figure 33: Dependence of mean stripe distance $l_{x,0}$ (red) on mean transfer velocity $v_{x,0}$ in comparison to the unforced system (blue). The data is taken from 2D direct numerical simulations. 1:1 and 1:2 synchronization lines are drawn as well according to Eq. ((49)).

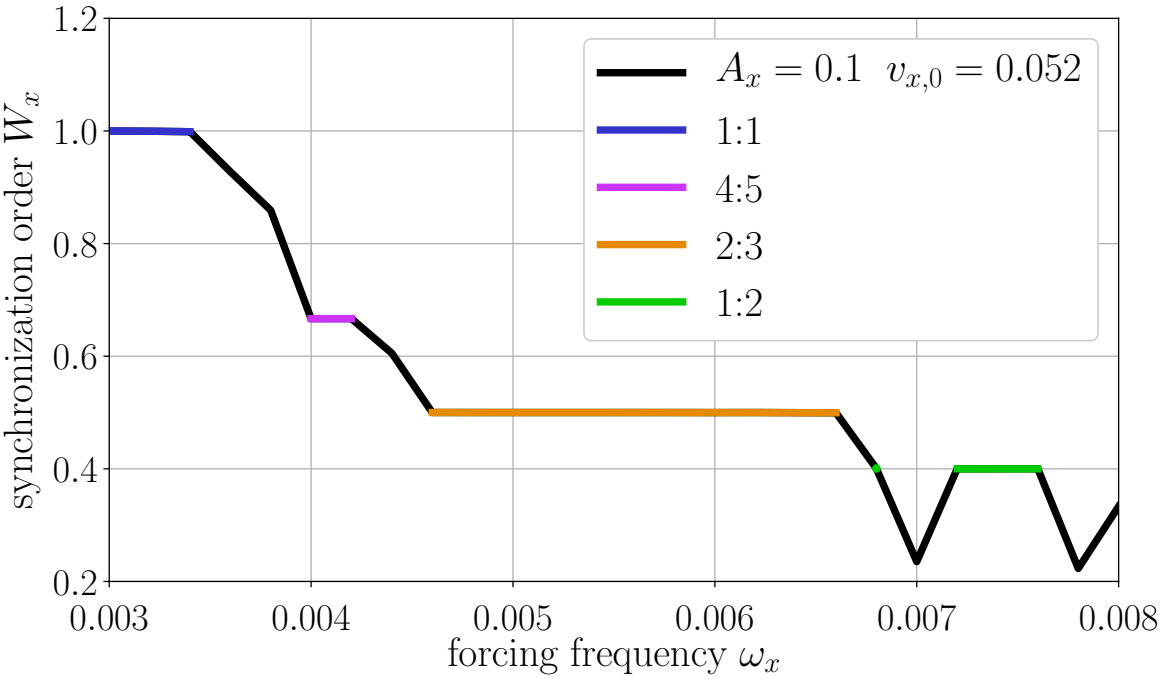

Figure 34: Dependence of synchronization order W_x on forcing frequency ω_x (black). The data is taken from 2D direct numerical simulations. The 1:1(blue), 4:5(purple), 2:3(orange) and 1:2(green) synchronization plateaus are marked as well.

5.2.2 Region of transversal instability

The velocity modulation is considered to be a temporal forcing term which acts in the vertical direction(x). And the spatial counterpart that comes to mind would be a prestructure. It was shown in [Wil16] that horizontally striped prestructures, or in other words spatial forcing in x-direction, suppress the transversal instability. This means that, as long as the spatial inhomogeneity in y of the initial condition is sufficiently small, horizontal stripes will form. If the inhomogeneity is large enough, transversal modes can grow and lead to vertical stripes or other patterns.

We first perform a parameter study in $v_{x,0}$ for $A_x \in \{0, 0.001, 0.01, 0.1\}$, $\omega_x = 0.002$ with initial condition as in Eq. (12) and noise. The resulting solutions are shown in Fig. 35. Parts of the parameter space are not shown since they simply represent continuations of neighboring patterns. For example the reader shall expect for $A_x = 0.001$, $v_{x,0} \in [0.026, 0.028]$ vertical stripes near the lower limit and horizontal ones towards the upper one. Furthermore, outside of the patterning regime LC and LE phase solutions emerge. Comparing the solutions for $A_x = 0$ and $A_x = 0.001$, we see that they behave very similarly. The system exhibits vertical stripes for $v_{x,0} = 0.026$ and horizontal ones in the rest of the patterning regime. For $A_x = 0.01$ a squared pattern emerges at $v_{x,0} = 0.033$. Finally, for $A_x = 0.1$ the region within which vertical stripes occur is shifted to lower velocities (here: $v_{x,0} = 0.024$) and is replaced by a branched pattern. At $v_{x,0} = 0.028$ we find an irregular lattice pattern. This will be clearer later on by comparing with Fig. 36. Something that can be observed independent of the amplitude is that towards the high velocity end of the patterning regime the horizontal stripes break up into smaller domains which are still horizontally aligned.

Three main observations can be made. The first one is the unsurprising extension of the patterning regime with increasing A_x. For example $A_x = 0.022$ still exhibits horizontal stripes while lower amplitudes already transition to a LE-solution. Next, the emergence of a square pattern at $A_x = 0.01$, $v_{x,0} = 0.033$ separated from vertical stripes at $A_x = 0.01$, $v_{x,0} =$

0.026 indicates multistability. This will be further investigated in the next section. Finally, the region of transversal instability increases with A_x (cf. $A_x = 0.1$, $v_{x,0} \in [0.024, 0.028]$). Thus, all in all temporal forcing as in Eq. (46) differs from spatial forcing via horizontally striped prestructures. The transversal instability is not suppressed but instead enhanced with increasing A_x. This is an important finding because the forcing only points in the $x - direction$ but can still affect transversal modes (k_y) by further destabilizing them.

5.2.3 Multistability

In order to confirm the existence of multistable regions another parameter study is done for the same parameters as in Sec. 5.2.2. The difference is that the calculations are done starting at $v_{x,0} = 0.026$ for $A_x = 0.001$ and $v_{x,0} = 0.024$ for $A_x = 0.1$ with the corresponding vertical stripes from the previous study found in Fig. 35 as initial conditions. $v_{x,0}$ is varied towards high and low velocities whereby taking the final solution of the previous calculation as the new initial condition for each set of new parameters. Part of the results are displayed in Fig. 36. This time the velocity steps are equidistant. The whole patterning regime is multistable, containing vertical stripes ($v_{x,0} = 0.024$), oblique patterns($A_x = 0.01$, $v_{x,0} = 0.028$), square patterns ($v_{x,0} = 0.032$), branched structures ($A_x = 0.1$, $v_{x,0} = 0.026$) and small, crudely horizontally aligned domains ($v_{x,0} = 0.040$). Horizontal stripes don't appear at all except for a few exceptions which will be discussed later. Fig. 36 is focused on the region where vertical and oblique stripes exist, while Fig. 36 is focused on the region of square patterns. Starting with Fig. 36 one can see that the region of stripes is shifted towards lower $v_{x,0}$ with increasing A_x. At $A_x = 0.1$ no oblique pattern can be observed anymore. Instead, branched structures and irregular lattice patterns emerge. Another interesting observation is the unusual square pattern for $A_x = 0.001$, $v_{x,0} = 0.022$. There, the squares consist of LE phase while the other square patterns exhibit LC phase as squares. The effect of shifting the pattern type towards lower velocities can be see in Fig. 36, too. There, the square patterns replace oblique patterns for increasing A_x. In turn, the square patterns are replaced at higher velocities by small, crudely horizontally aligned domains.
One can explain this behavior by looking at the number of modes for each pattern type. Vertical stripes are made of one mode that only has a k_y-component and no k_x-component. Oblique patterns are also made of one mode but both components are nonzero. Square patterns consist of two modes, each with nonzero k_y and k_x-components, resulting in a total of two nonzero k_x-components if we do not count the complex conjugates. Since the transfer occurs in the x-direction, an increase in A_x naturally allows modes in x-direction to grow easier. Oblique stripes turn into squares, vertical stripes turn into oblique ones.
For velocities higher than the ones displayed in Fig. 36 the patterns from $v_{x,0} = 0.04$ just continue and then transition to LE-solutions. But for high amplitude $A_x = 0.1$ there are regions where these patterns stabilize and form horizontal stripes ($v_{x,0} = 0.042, 0.044, 0.054, 0.056$, not shown here). In order to further confirm this stabilization another calculation is done with vertical stripes as the initial condition and $A_x = 0.1$, $\omega_x = 0.002$, $v_{x,0} = 0.042$. The resulting time-series is shown in Fig. 37. We can see how the vertical stripes destabilize and are replaced by horizontal ones. Hysteresis effects have not been investigated and may be object of future studies.
Taking into account the previous statement that the time-periodic forcing increases the region of transversal instability there has to be an optimal forcing amplitude A_x which cannot be too high because it would stabilize horizontal stripes again at some point.

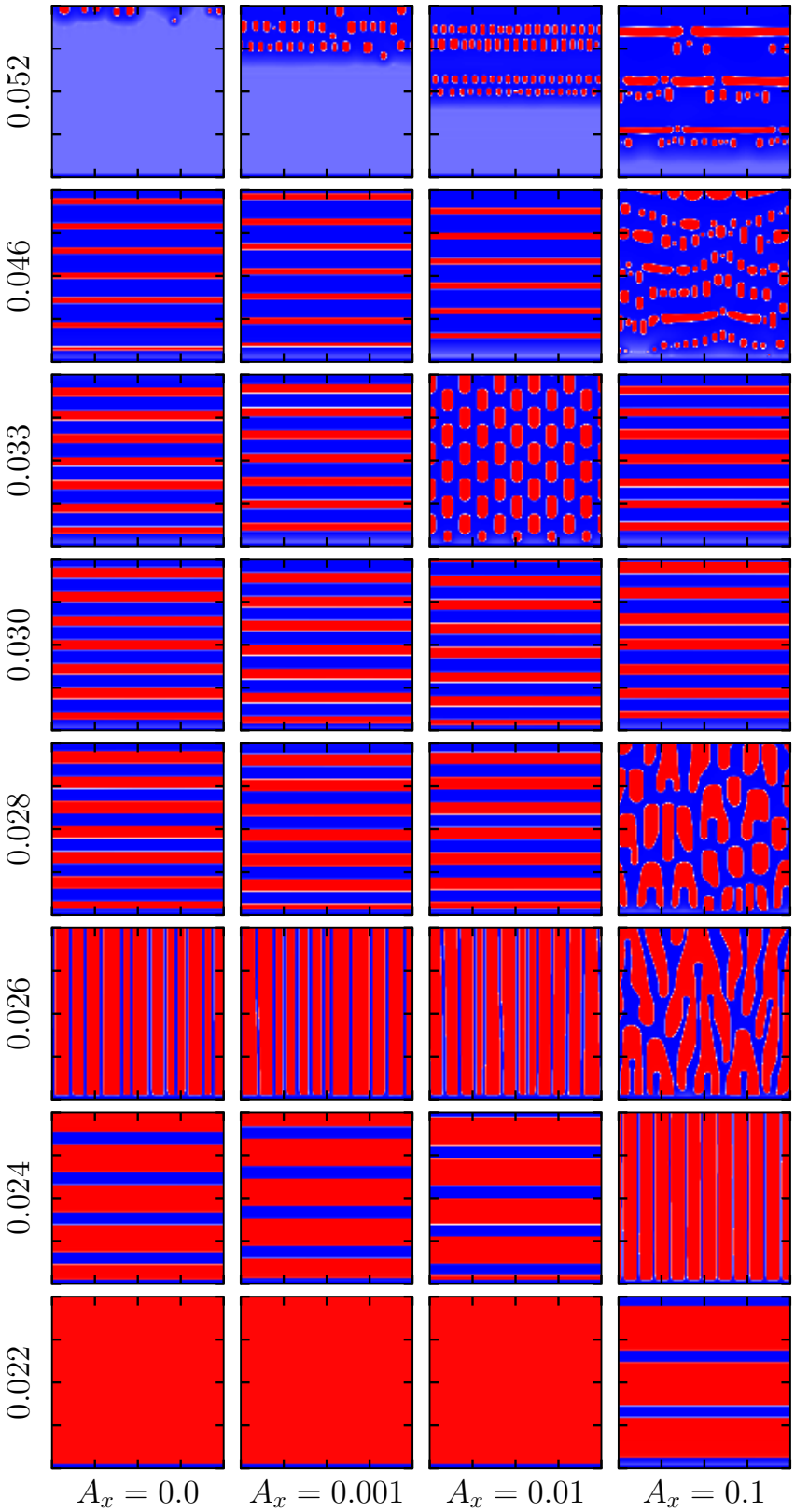

Figure 35: 2D solutions of (9) with time-periodic forcing as in Eq. (46) with initial condition as in Eq. (12) with noise, obtained from direct numerical calculations. The forcing amplitude A_x is increased from left to right while the mean transfer velocity $v_{x,0}$ is increased from bottom to top, $\omega_x = 0.002$. Note that the displayed solutions are not equidistant regarding $v_{x,0}$.

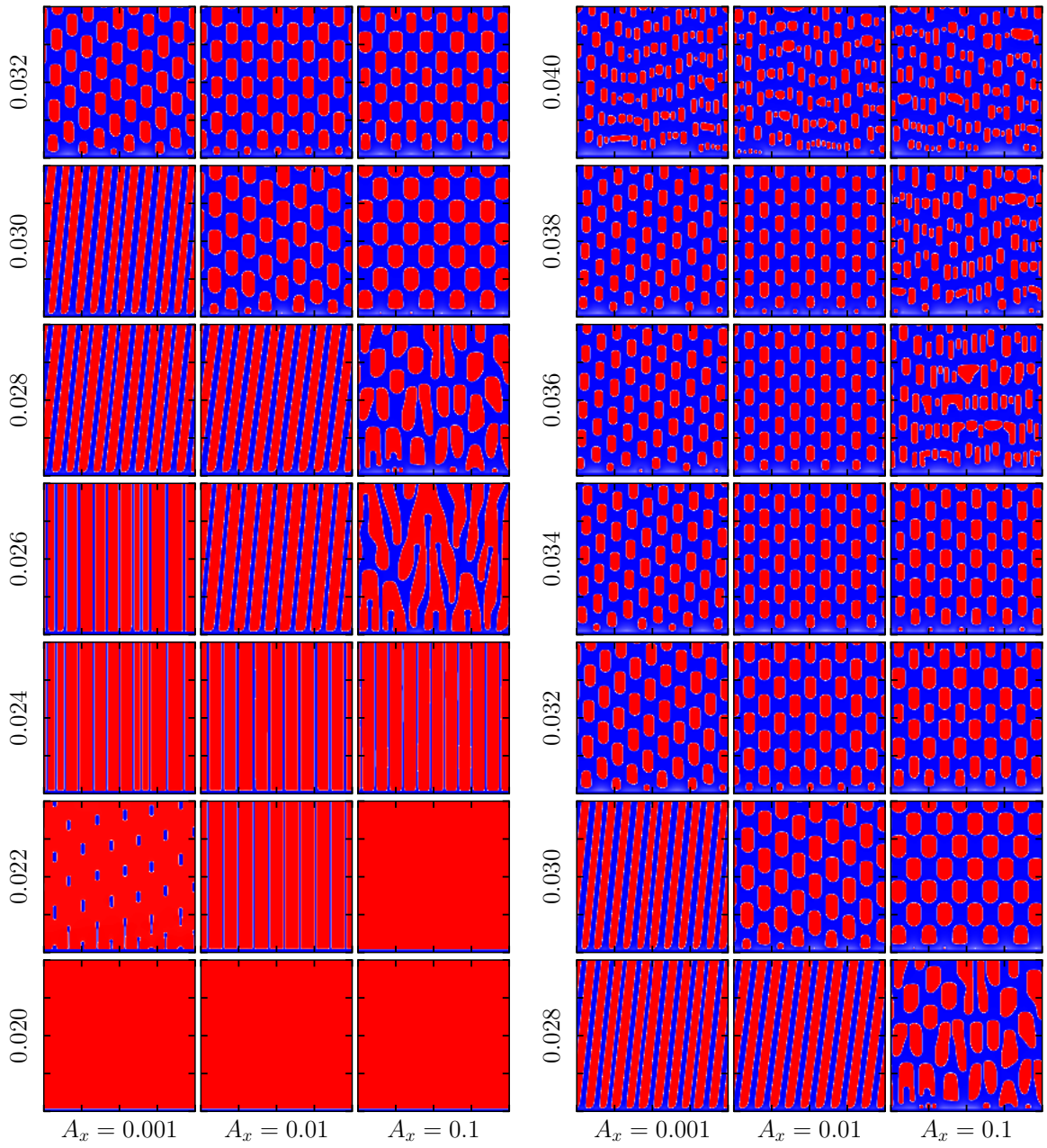

Figure 36: 2D solutions of Eq. (9) with time-periodic forcing as in Eq. ((46)), obtained from direct numerical calculations. The very first run ($v_{x,0} = 0.026$ or $v_{x,0} = 0.024$) for each A_x is done with vertical stripes as the initial condition. After that the final solution of the previous calculation is chosen as the new initial condition for the new parameter set. The forcing amplitude A_x is increased from left to right while the mean transfer velocity $v_{x,0}$ is increased from bottom to top, $\omega_x = 0.002$.

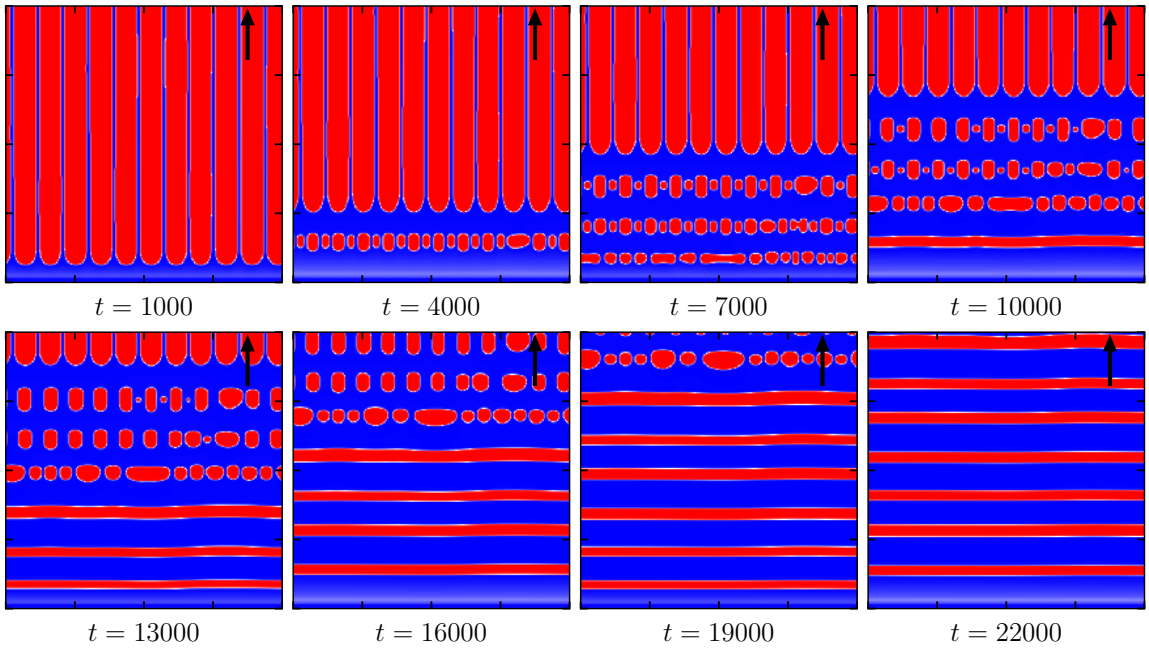

Figure 37: Time-series of 2D solutions of Eq. (9) with vertical stripes as initial conditions. $A_x = 0.1$, $\omega_x = 0.002$, $v_{x,0} = 0.042$.

5.2.4 Branched pattern

Looking back at Fig. 36 one might suspect the branched solution at $A_x = 0.1$, $v_{x,0} = 0.026$ to have not fully converged yet. The said pattern is plotted once again in Fig. 38. In addition, the time evolution of the L^2-norm is examined in Fig. 40. L^2 is calculated at equidistant times t_n. The norm behaves irregularly. One would expect a periodic behavior for a converged periodic solution or saturation if a stationary solution is reached. Neither of these are the case. Thus, the long-term solution either perpetually behaves like this or is still in a long-time transient state. Note that the relative standard deviation lies at $\frac{\sigma(L^2)}{<L^2>} = 0.36\%$.

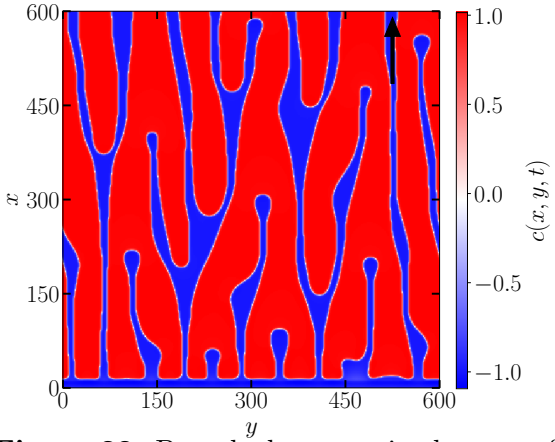

Figure 38: Branched pattern in the case of time-periodic forcing $A_x = 0.1$, $\omega_x = 0.002$, $v_{x,0} = 0.026$. Blue parts represent LE phase and red represents LC.

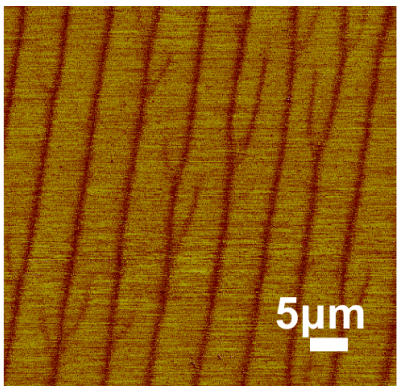

Figure 39: AFM image of branched pattern obtained for LB transfer with constant velocity. Dark brown branches represent LE phase and light brown LC ([ZWH+16]).

In either case the branched pattern resembles branched patterns observed in LB transfer experiments quite well. Next to Fig. 38 an AFM image of a branched pattern measured for

LB transfer with constant transfer velocity is shown (Fig. 39). There, dark brown branches represent LE phases. Thus, they need to be compared to the blue branches in Fig. 38. This leads to the conjecture that branched patterns observed in experiments might be transient states.

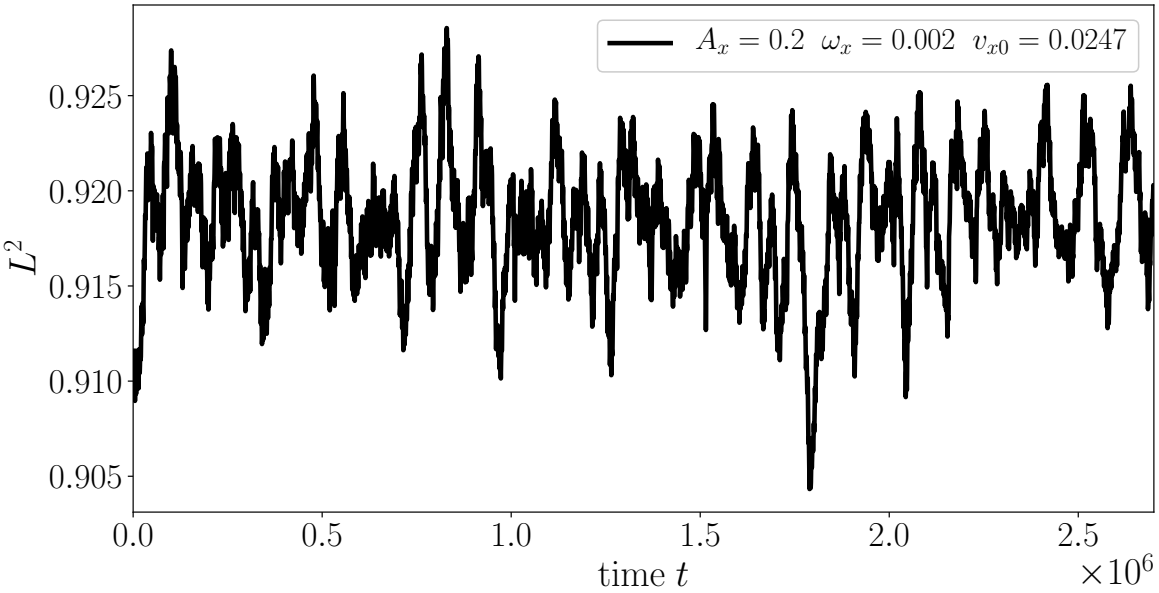

Figure 40: Time evolution of L^2-norm of branched pattern seen in Fig. 38 with time-periodic forcing $A_x = 0.1$, $\omega_x = 0.002$, $v_{x,0} = 0.026$.

5.2.5 Transversally modulated vertical stripes

It was shown in Sec. 5.2.1 that horizontal stripes exhibit synchronization effects with the incorporation of temporal forcing. And since the forcing is able to affect the y-direction by enhancing the region of transversal instability, it should be possible for patterns which are inhomogeneous in y to synchronize, too. In the region of vertical stripes it is possible to find solutions whose stripes are periodically and transversally modulated. This results in a sort of "pulsing" of the stripes. A good example is shown on the left side in Fig. 41 for $A_x = 0.2$, $\omega_x = 0.002$, $v_{x,0} = 0.0244$. One could measure the stripe distances just like in previous calculations in order to determine the synchronization order W_y, W_x for different directions. But a more visually accessible method is applying a fourier transform on the pattern. It is plotted on the right side in Fig. 41. Instead of the wavenumbers k_y and k_x, the synchronization orders W_y and W_x for the y- and x- directions are chosen for the two axes. This is because (cf. Eq. (49))

$$W = \frac{l_f}{l_0} = \frac{k_0}{k_f} = k_0 \frac{\omega}{v_0}. \tag{51}$$

k_0 is the wavenumber corresponding to the mean stripe distance l_0 and k_f is the one corresponding to the forced stripe distance l_f. Looking at the local maxima of $\mathcal{F}[c]$ we observe three modes with their respective complex conjugates. One mode has a vanishing x-component. The corresponding synchronization order is $W_y = 1.5$ and its multiples (not shown), meaning that the mode which is responsible for the vertical stripes is synchronized by 3:2 to the time-periodic forcing. The remaining two modes (very light, gray local maxima) are synchronized by 4:3 ($W_x = 0.75$) in the horizontal direction and 1:2 ($W_y = 0.5$) in the vertical direction. The pulsing is in fact caused by the superposition of a squared pattern with vertical stripes. One can imagine that for smaller amplitudes the modes for the squares are not yet existent and the vertical stripes are synchronized by 4:3. Then, by increasing the amplitude, part of

the vertical stripes mode gains x-components, caused by the forcing, finally resulting in this "pulsing" pattern.
This parameter set has also been tested for higher discretization $L_x = L_y = 600$, $N_x = N_y = 448$. The pattern does not change. Therefore, the modulation is not an artifact of the discretization.

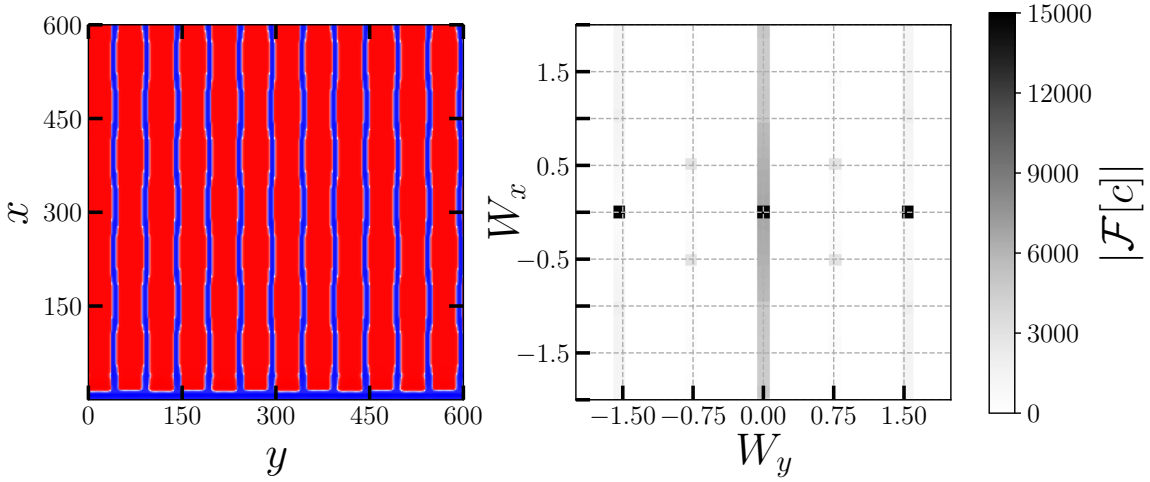

Figure 41: Left: Transversally modulated vertical stripes in the case of time-periodic forcing with $A_x = 0.2$, $\omega_x = 0.002$, $v_{x,0} = 0.0244$. Right: Fourier transform $\mathcal{F}[c]$ of the pattern with synchronization orders W_y, W_x as axes (cf. Eq. (51)).

6 Conclusion and Outlook

By introducing time-periodic forcing as in Eq. (46) into the transfer velocity in the specific Cahn-Hilliard model (Eq. (9)) it was shown that most synchronization phenomena expected for time-periodic forcing can be observed in the system. By deriving an equation that relates the forcing frequency ω to the mean stripe distance l_0 it is possible to characterize regions of synchronization in parameter space. l_0 depends linearly on the mean transfer velocity v_0 and inverse on the forcing frequency ω within regions of synchronization.
The forcing extends the original pattern regime of the unforced system towards higher transfer velocities. In addition, by choosing small forcing frequencies it is possible to extend the patterning regime towards smaller velocities as well.
Outside of the patterning regime of the unforced system the forced system clearly exhibits common synchronization orders like 1:1, 2:1 or 2:3. While inside the original patterning regime the system takes on synchronization orders which correspond to stripe lengths close to the natural one. Note that increasing the forcing amplitude extends the synchronization regions from outside the original patterning regime into it.
By means of parameter studies characteristic figures like the Devil's staircase and Arnold tongues are calculated. Thereby confirming further synchronization behavior, e.g. expansion of synchronization regions by increasing the forcing amplitude or by adjusting the frequency closer to the natural one. We also observe the preference of synchronization orders comprised of low integer values. Furthermore, the extensive parameter studies in v_0 and ω reveal an even wider variety of synchronization orders allowing more possibilities regarding control of the stripe distance.
However, one needs to be careful when talking about synchronization of the stripe distance. It is always the mean which is synchronized. The individual stripe distances vary in time and can be for example two- or four-periodic. On the other hand it has been shown that 1:n synchronized states usually exhibit just one stripe distance.
A short study on the duty cycle depending on v_0 reveals that it strongly follows the duty cycle of the unforced system but immediately locks onto other synchronization orders once it reaches the end of the original patterning regime. The dependency on ω does not show any simple behavior.
2D simulations reveal very similar synchronization effects to the 1D case when considering horizontal stripes. But once transversal inhomogeneity is introduced to the system, it exhibits patterns like vertical stripes, lattice structures or branched structures. The transversal instability is not suppressed like in the case of horizontally striped prestructures and we find large regions of multistability. Note, that increasing the amplitude increases the region of transversal instability but too large of an increase leads to suppression of the instability again. Observed branched structures remind the observer of similar structures in real experiments leading to the possibility of the experimental patterns being transient states. Finally, synchronization effects can also be observed in the 2D case with horizontal inhomogeneity. The particular example is a vertically striped pattern that is modulated in the transversal direction, exhibiting synchronization in both spatial directions.
There are still multiple aspects that can be studied in the time-periodically forced system. The main aspect being further synchronization behavior when introducing horizontal inhomogeneity. Further, the behavior of individual stripes has yet to be analyzed in a systematic manner. Lastly, the system will be studied with continuation methods in the future in order to verify the findings and to use another investigation tool.

References

[Blo34] K. B. Blodgett. Monomolecular films of fatty acids on glass. *Journal of the American Chemical Society*, 56(2):485, 1934.

[Blo35] K. B. Blodgett. Films Built by Depositing Successive Monomolecular Layers on a Solid Surface. *J. Am. Chem. Soc.*, 57:1007–1022, 1935.

[But08] J. C. Butcher. *Numerical Methods for Ordinary Differential Equations*. John Wiley & Sons, 2008.

[CLH+] X. Chen, S. Lenhert, M. Hirtz, N. Lu, H. Fuchs, and L. Chi. Langmuir-Blodgett Patterning: A Bottom-Way to Build mesostrcutures over Large Areas. *Acc. Chem. Res.*, 40:393–401.

[DFSA08] G. Delon, M. Fermigier, J. H. Snoeijer, and B. Andreotti. Relaxation of a dewetting contact line Part 2: Experiments. *J. Fluid Mech.*, 604:55–75, 2008.

[DP80] J. R. Dormand and P.J. Prince. A family of embedded Runge-Kutta formulae. *Journal of Computational and Applied Mathematics*, 6(1):19–26, 1980.

[Feh69] E. Fehlberg. Klassische Runge-Kutta-Formeln vierter und niedrigerer Ordnung mit Schrittweiten-Kontrolle und ihre Anwendung auf Wärmeleitungsprobleme. *Computing*, 4:93–106, 1969.

[GR96] K. Graf and H. Riegler. Molecular adhesion interactions between Langmuir monolayers and solid substrates. *Colloids Surf.*, 131:215–224, 1996.

[HLL+09] J. Henzie, J. Lee, M. H. Lee, W. Hasan, and T. W. Odom. Nanofabrication of Plasmonic Structures. *Annu. Rev. Phys. Chem.*, 60:147–165, 2009.

[IO00] T. Ito and S. Okazaki. Pushing the limits of lithography. *Nature*, 406:1027–1031, 2000.

[KGFC10] M. H. Köpf, S. V. Gurevich, R. Friedrich, and L. Chi. Pattern Formation in Monolayer Transfer Systems with Substrate - Mediated Condensation. *Langmuir*, 26(13):10444–10447, 2010.

[KGFT12] M. H. Köpf, S. V. Gurevich, R. Friedrich, and U. Thiele. Substrate-mediated pattern formation in monolayer transfer: a reduced model. *New J. of Physics*, 14:023016, 2012.

[KT14] M. H. Köpf and U. Thiele. Emergence of the bifurcation structure of a Langmuir-Blodgett transfer model. *Nonlinearity*, 27:2711–2734, 2014.

[Lan34] I. Langmuir. Mechanical Properties of Monomolecular Films. *Journal of the Franklin Institue*, 218(2):143–171, 1934.

[LBM00] S. Leporatti, G. Brezesinski, and Möhwald. Coexistence of phases in monolayers of branched-chain phospholipids investigated by scanning force microscopy. *Colloids Surf.*, 161:159–171, 2000.

[NCS84] A. Novick-Cohen and L. A. Segel. Nonlinear Aspects of The Cahn-Hilliard Equation. *Physica D*, 10:277–298, 1984.

[NVI17] NVIDIA. CUDA C Programming Guide Version 8.0, 2017.

[Ozb06] E. Ozbay. Plasmonics: Merging Photonics and Electronics at Nanoscale Dimensions. *Science*, 311(5758):189–193, 2006.

[PRK01] A. Pikovsky, M. Rosenblum, and J. Kurths. *Synchronization: A universal concept in nonlinear science*. Cambridge University Press, Cambridge, 2001.

[PS12] A. Pimpin and W. Srituravanich. Review on Micro- and Nanolithography Techniques and their Applications. *Engineering Journal*, 16:37–56, 2012.

[RP03] M. Rosenblum and A. Pikovsky. Synchronization: from pendulum clocks to chaotic lasers and chemical oscillators. *Contemporary Physics*, 44(5):401–416, 2003.

[SADF07] J. H. Snoeijer, B. Andreotti, G. Delon, and M. Fermigier. Relaxation of a dewetting contact line. Part 1: A full-scale hydrodynamic calculation. *J. Fluid Mech.*, 579:63–83, 2007.

[SCR93] K. Spratte, L. Chi, and H. Riegler. Physisorption Instabilites during Dynamic Langmuir Wetting. *Europhys. Lett.*, 25(3):211–217, 1993.

[WG14] M. Wilczek and S. V. Gurevich. Locking of periodic patterns in Cahn-Hilliard models for Langmuir-Blodgett transfer. *Phys. Rev. E*, 90:042926, 2014.

[Wil82] S. D. R. Wilson. The drag-out problem in film coating theory. *J. Engg. Math.*, 16:209–221, 1982.

[Wil12] M. Wilczek. Pattern formation in Cahn-Hilliard models for Langmuir-Blodgett transfer. Master's thesis, Westfälische Wilhelms-Universität Münster, 2012.

[Wil16] M. Wilczek. *Pattern formation in Driven Thin Layers of Simple and Complex Liquids*. Dissertation, Westfälische Wilhelms-Universität Münster, 2016.

[WJ04] S. J. Weinstein and Ruschak K. J. Coating Flows. *Annu. Rev. Fluid Mech.*, 36:29–53, 2004.

[YRP+05] E. K. F. Yim, R. M. Reano, S. W. Pang, A. F. Yee, C. S. Chen, and K. W. Leong. Nanopattern-induced changes in morphology and motility of smooth muscle cell. *Biomaterials*, 26:5405–5413, 2005.

[ZWH+16] J. Zhu, M. Wilczek, M. Hirtz, J. Hao, W. Wang, H. Fuchs, and S. V. Gurevich. Branch Suppression and Orientation Control of Langmuir-Blodgett Patterning on Prestructured Surfaces. *Adv. Mater. Interf.*, 3:1600478, 2016.

Declaration of Authorship

I hereby confirm that I have authored this Master's thesis independently and without use of others than the indicated sources. All passages which are literally or in general matter taken out of publications or other sources are marked as such.

Mnster, September 28, 2017